SMAC mimetics overcome apoptotic resistance in ovarian cancer through MSLN-TNF alpha axis

Authors:

Coelho Ricardo[1], Seashore-Ludlow Brinton[2], Schütz Sarah[1], Lombardo Christopher Flavio[1], Moussaud-Lamodière Elisabeth[2], Casanova Ruben[3,4], Ficek-Pascual Joanna[4], Labrosse Brunhilde Kathrin[1,5], Lopez-Nunez Monica[1], Rimmer Natalie[1], Fedier Andre[1], Lima Renata[1], Montavon Sartorius Céline[5,6], Kurzeder Christian[5,7], Singer Franziska[8,9], Bertolini Anne[8,9], Tumor Profiler Consortium, Rätsch Gunnar[4], Bodenmiller Bernd[3], Kallioniemi Olli[2], Östling Päivi[2], David Leonor[10,11,12], Heinzelmann-Schwarz Viola[1,5,6*], Jacob Francis[1*]

Affiliations:

1. Ovarian Cancer Research, Department of Biomedicine, University Hospital Basel and University of Basel, Basel, Switzerland
2. Department of Oncology and Pathology, Science for Life Laboratory, Karolinska Institute, Solna, Sweden
3. Department of Quantitative Biomedicine, University of Zürich, Switzerland
4. Department of Computer Science, Eidgenössische Technische Hochschule (ETH) Zürich, Zürich, Switzerland
5. Gynaecological Cancer Centre, University Hospital Basel and University of Basel, Basel
6. Hospital for Women, University Hospital Basel, Basel, Switzerland
7. Breast Center, University Hospital Basel, Basel, Switzerland
8. SIB Swiss Institute of Bioinformatics, Basel, Switzerland
9. ETH Zurich, NEXUS Personalized Health Technologies, Schlieren, Switzerland
10. Institute of Molecular Pathology and Immunology of the University of Porto (IPATIMUP), Porto, Portugal.
11. Faculty of Medicine, University of Porto, Porto, Portugal
12. Institute for Research and Innovation in Health (i3S) of the University of Porto

*equal contribution

Keywords: chemoresistance, live cell imaging, myeloid cells, patient- derived cultures, programmed cell death, targeted therapy, TNF alpha signaling

Abstract

Resistance to chemotherapy and PARPi inhibitors remains a critical challenge in the treatment of epithelial ovarian cancer, mainly due to disabled apoptotic responses in tumor cells. Given mesothelin's pivotal role in ovarian cancer and its restricted expression in healthy tissues, we conducted a drug-screening discovery analysis across a range of genetically modified cancer cells to unveil mesothelin's therapeutic impact. We observed enhanced cell death in cancer cells with low mesothelin expressing when exposed to a second mitochondria-derived activator of caspases (SMAC) mimetics, and demonstrated a compelling synergy when combined with chemotherapy in *ex vivo* patient-derived cultures and zebrafish tumor xenografts. Mechanistically, the addition of the SMAC mimetics drug birinapant to either carboplatin or paclitaxel triggered the activation of the Caspase 8-dependent apoptotic program facilitated by TNFα signaling. Multimodal analysis of neoadjuvant-treated patient samples further revealed an association between tumor-associated macrophages and the activation of TNFα-related pathways. Our proposed bimodal treatment shows promise in enhancing the clinical management of patients by harnessing the potential of SMAC mimetics alongside conventional chemotherapy.

Introduction

Primary debulking surgery followed by platinum-based chemotherapy has been the cornerstone treatment for advanced high-grade serous ovarian cancer (HGSOC) for decades *(1, 2)*. In recent years, maintenance therapies including poly (ADP-ribose) polymerase inhibitors (PARPi), have become a valuable addition in patients with somatic or germline *BRCA1/2* tumors or homologous recombination deficiency (HRD), *(3–6)*. Despite these therapeutic advancements, most patients with metastatic HGSOC inevitably experience disease recurrence and ultimately platinum-resistance disease *(7)*. Considering these challenges, the necessity for overcoming drug resistance remains a critical clinical priority for these patients.

A growing body of evidence indicates that mesothelin (MSLN), a glycoprotein physiologically expressed at the surface of mesothelial cells lining the peritoneal cavity and overexpressed in several malignancies *(8–10)* plays a central role in tumor progression *(11–14)*. Additionally, we identified MSLN as a key player in the multistep process of metastasis in EOC, where it promotes cell survival in suspension, invasion through the mesothelial cell layer, and peritoneal spread *(15)*. Given its restricted expression and its role in ovarian cancer progression, MSLN has emerged as a promising candidate for targeted therapies using either antibody-based conjugates *(16, 17)* or CAR-T cell therapies *(18, 19)*. Currently, several clinical trials (NCT02792114, NCT03816358, NCT04809766, NCT03814447, NCT03054298) are underway to assess the potential of these targeted therapies in combination with chemotherapy, an area that holds promise for preventing or overcoming drug resistance.

Despite the increasing promise of MSLN-targeted therapies in HGSOC, a notable gap exists in our understanding, particularly regarding the broader role of MSLN in overall drug responses, including its specific impact on chemotherapy responses. To fill this knowledge gap, we functionally address the question by conducting a comprehensive drug library screen on genetically manipulated cell lines with varying levels of MSLN expression. Furthermore, we identify drug synergies, specifically combining carboplatin or paclitaxel with SMAC mimetics (bimodal treatment) through a TNFa-caspase-8 dependent mechanism.

Results

Ovarian cancer cells with low MSLN expression are selectively targeted by SMAC mimetics

MSLN expression has been correlated with chemoresistance *(20,21,22)*. However, these studies primarily report on associations without functionally elucidating the role of MSLN in drug responses. To fill this gap, we utilized our previously established experimental model *(15)*, consisting of isogenic EOC cell lines with genetically manipulated MSLN expression, to a comprehensive drug sensitivity and resistant test (DSRT) comprising a 528 oncology drug library including kinase inhibitors, epigenetic modifiers, differentiating agents, and conventional chemotherapeutic compounds (CHEMICAL COMPOUND LIBRARIES, **Supplementary Table 1**). We evaluated cellular response to treatment by calculating the drug sensitivity score (DSS, *(23)*), which revealed a diverse spectrum across all cell lines tested (n=8). Despite marginal differences in DSS to conventional chemotherapeutics (**Figure 1A-B**), we identified SMAC mimetics as exhibiting a selective effect on $MSLN^{low/\Delta MSLN}$ EOC cell lines (**Figure 1C**). This increased sensitivity to SMAC mimetics was further validated for the SMAC mimetic drug birinapant in two EOC cell lines genetically engineered for MSLN expression, either by MSLN knockout ($OVCAR3^{\Delta MSLN}$) or overexpression (OVCAR4 OE MSLN) (**Figure 1D**). To further prove the MSLN-specific response to SMAC mimetics, we conducted a co-culture time-lapse experiment exposing parental ($MSLN^{high}$) and *ΔMSLN* OVCAR3 cells to birinapant treatment. For cell death assessment, we employed POPO™-1 iodide, a nontoxic cell impermeant dye. We observed a significant increase in cell death for *ΔMSLN* compared to parental OVCAR3, supporting the hypothesis that SMAC mimetics preferentially target $MSLN^{\Delta MSLN}$ cells (**Figure 1E**). The tumor microenvironment (TME) plays a crucial role in modulating drug responses *(24)*. Mesothelial cells represent a major cellular component of the peritoneal microenvironment, the location where EOC cells are predisposed to metastasize *(25–28)*. Recognizing the importance of mesothelial cells in cancer progression and drug responses, we assessed the efficacy of birinapant in a co-culture assay using aggregates of parental and *ΔMSLN* OVCAR3 alongside normal immortalized mesothelial cells (MeT5A). This co-culture assay unveiled a selective effect of birinapant on *ΔMSLN* OVCAR3 cells, with minor effects on the MeT5A cell viability (**Figure 1F**). Taken together, our data indicates that the SMAC mimetics selectively targets $MSLN^{low/\Delta MSLN}$ EOC cells.

SMAC mimetics restore chemotherapy sensitivity

Despite observing marginal differences in the cellular response to carboplatin and paclitaxel chemotherapeutics when comparing the DSS values among cell lines with differential MSLN expression, we hypothesized that chemotherapy might induce changes in MSLN levels. This hypothesis is based on the well-documented effect of chemotherapeutic agents in inducing cellular alterations, including DNA damage *(29)*, and cell cycle arrest *(30)*. These alterations

113 ultimately lead to extensive modifications in gene expression and protein function *(31, 32)*. Thus,
114 we screened a panel of 18 EOC cell lines for MSLN expression and selected representative ones
115 with MSLN^{high} expression for downstream assays (**Supplementary Figure 1A**). Following
116 exposure to a gradient concentration of carboplatin and paclitaxel, the most effective
117 chemotherapy compounds in EOC, we observed a decrease in MSLN protein levels across all
118 cell lines tested (n=4). This reduction was accompanied by reduced cell viability, as evidenced by
119 the increased expression of cleaved PARP (**Figure 2A, Supplementary Figure 1B**). The
120 treatment of chemotherapy carboplatin with paclitaxel had a less pronounced impact on MSLN
121 protein levels as if they were given as single compounds (**Supplementary Figure 1C**). Given this
122 finding, we proceeded with downstream experiments using only the combination of SMAC
123 mimetics with either carboplatin or paclitaxel. Of note, EOC cell lines used exhibited a general
124 resistance to carboplatin and paclitaxel (**Supplementary Figure 1D**).
125 Supported by the observed reduction in MSLN protein levels following exposure to either
126 carboplatin or paclitaxel and the specificity of SMAC mimetics in targeting MSLN^{low} cancer cells,
127 we conducted a dose-response matrix test and assessed the synergy scores for either carboplatin
128 or paclitaxel in combination with SMAC mimetics (birinapant and LCL161) in a panel of EOC cell
129 lines (n=6). We found enhanced MSLN-dependent drug efficiency when combining one
130 chemotherapeutic compound (either carboplatin or paclitaxel) with a SMAC mimetic (bimodal
131 treatment) (**Figure 2B**). To systematically analyze drug interaction patterns, we next employed
132 the Zero Interaction Potency (ZIP) model *(33, 34)*. This analysis revealed additive and synergistic
133 effects for the bimodal treatments in six EOC cell lines tested in an MSLN-dependent manner.
134 Surprisingly, the clinically routine combination of carboplatin with paclitaxel exhibited only a low
135 interaction pattern compared to applied bimodal treatments. (**Figure 2C and D and**
136 **Supplementary Figure 2**).
137 To further validate the synergistic effects, we profiled five HGSOC samples exhibiting high MSLN
138 expression for *ex vivo* drug testing (**Supplementary Figure 3A and Supplementary Table 2**).
139 These samples exhibited ubiquitous *TP53* mutations and heterogeneous mutation patterns in HR
140 and other frequently altered HGSOC genes (**Figure 2E, Supplementary Table 3**). The dose-
141 response matrix demonstrated a remarkable increase in the efficiency of SMAC mimetics in
142 combination with either carboplatin or paclitaxel. We found additive and synergistic interactions
143 of bimodal treatments for three out of five HGSOC patient-derived samples tested, importantly,
144 independent of the tumor cell content (**Figure 2F and supplementary Figures 3B and C**). To
145 assess the on-target tumor effect of the bimodal treatment, we next utilized a scaffold-free 3D *ex*
146 *vivo* culture system followed by immunofluorescence staining for E-cadherin and cleaved caspase
147 3 (cCASP3). A significant increase in the percentage of apoptotic tumor cells was observed for
148 the bimodal treatments as compared with controls suggesting a cancer cell-specific killing effect
149 (**Figures 2G and H**). Cellular responses to our bimodal treatment were also assessed using the

150 zebrafish embryo tumor xenograft model. In this model, we transplanted COV362 MSLN^{high} cells
151 (carboplatin and paclitaxel-resistant) stably expressing dTomato fluorescent protein
152 (COV362_Chili) into transgenic *Tg(kdrl:eGFP)* zebrafish embryos *(35, 36)*. Zebrafish embryos
153 were then exposed to birinapant in combination with paclitaxel or to the vehicle for 72 hours. The
154 bimodal treatment significantly (p=0.021) reduced the percentage of viable COV362_Chili (DAPI^{-}
155) cells as compared with the control condition (DMSO) (**Figure 2I)**. Additionally, to exclude any
156 potential toxicity arising from off-target effects of the bimodal treatment, zebrafish embryos were
157 exposed to a gradient concentration of paclitaxel, birinapant, and their combinations for 72 hours.
158 Neither the mortality rate, malformations, missing organs, organ deficiencies, nor altered mobility
159 capacity were observed in zebrafish larvae exposed to the different drugs and combinations,
160 indicating low off-target toxicity of the tested compounds (**Supplementary Figure 4**). In summary,
161 these results suggest that SMAC mimetics administered with either carboplatin or paclitaxel
162 enhance tumor cell killing *in vitro*, *ex vivo*, and *in vivo* while causing minimal off-target toxicity.
163
164 ***Birinapant promotes cancer cell apoptosis through TNFα signaling***
165 SMAC mimetics have gained attention as a promising class of targeted therapies and are
166 currently under clinical investigation for both solid and hematological malignancies *(37)*.
167 Mechanistically, SMAC mimetics are suggested to bind to Baculovirus Inhibitor apoptotic proteins
168 Repeat domains (BIR) of Inhibitor of Apoptosis (IAP)s, activating NF-κB signaling pathway and,
169 induction of cell death in a TNFα-dependent manner *(38–40)*. However, the detailed mechanism
170 of action of SMAC mimetics, particularly regarding their synergistic effects when combined with
171 either carboplatin or paclitaxel, remains unclear. To assess the impact of TNFα signaling on drug
172 synergies, we exposed MSLN^{high} EOC cell lines (Kuramochi and OVCAR3) to the bimodal
173 treatments in the presence of a neutralizing TNFα antibody or supplementing the culture medium
174 with human recombinant TNFα protein. The results demonstrated that birinapant, used alone or
175 in combination with either carboplatin or paclitaxel, significantly enhanced cancer cell death in a
176 TNFα-dependent manner (**Figure 3A and B and Supplementary Figure 5A-C**). This was
177 supported by the significant increase in the *TNFA* expression in EOC cells after exposure to
178 carboplatin, paclitaxel, birinapant, and bimodal treatment (**Supplementary Figure 5D**). Of note,
179 the major target of SMAC mimetics, cellular (c)IAP1 protein *(39)*, exhibited a cell line-dependent
180 protein expression after applied treatments (**Figure 3B and Supplementary Figure 5C and E**).
181 These data suggest that birinapant may target different IAP proteins in a cell line-dependent
182 manner, yet consistently produces an enhanced effect when combined with either carboplatin or
183 paclitaxel.
184 SMAC mimetics have been reported to trigger cell death through distinct programmed cell death
185 (PCD) pathways, involving either caspase-dependent apoptosis or caspase-independent
186 necroptosis *(41–45)*. The induction of these different pathways of PCD depends on the specific

187 combination of SMAC mimetics and the cancer model under investigation *(41, 43, 46, 47)*. To
188 evaluate which PCD is induced by our bimodal treatments in EOC, we established a reporter for
189 Caspase 3 and 8 activity, leveraging a previously introduced FLIP-GFP system *(48)*. Both reporter
190 systems were validated by either immunofluorescence staining or pharmacological inhibition (Z-
191 IETD-FMK) for Caspase 3 and 8, respectively (**Supplementary Figure 6A and B**).
192 Flow cytometry data from Kuramochi and OVCAR3 cells, which stably expressed caspase
193 reporters, demonstrated a significant increase in Caspase 8 and 3 activities (EGFP+) when TNFα
194 supplementation was provided, either in combination with birinapant or as part of our bimodal
195 treatments. Importantly, the increase in caspase activity was specifically induced by
196 supplementation with TNFα and not by the IFNγ (**Figure 3C and D, Supplementary Figure 6C**).
197 To further validate apoptosis as the primary PCD pathway responsible for the observed synergies,
198 and to investigate the role of the NF-κB pathway in the outcome of bimodal treatment, we
199 conducted a CRISPR-Cas9 cell competition assay *(49)* in OVCAR3 cells. In this assay, we
200 targeted *NIK*, *IKKb*, *CASP8*, and *RIPK3* genes, encoding key players in the non-canonical and
201 canonical NF-κB pathway, apoptosis, and necroptosis, respectively. The generated data support
202 the finding that apoptosis is indeed the primary PCD pathway triggered by the treatment with
203 TNFα, birinapant, and birinapant in combination with paclitaxel. This was evidenced by the
204 increased cell resistance to these treatments upon genetic deletion of *ΔCASP8* (**Figure 3E**).
205 Enhanced sensitivity to the bimodal treatment- (birinapant/ paclitaxel) was also observed in *ΔKKb*
206 *and ΔIKKb* indicating the additional involvement of the NF-κB signaling pathway in the treatment
207 response. The role of Caspase 8 in mediating cell death upon the bimodal treatment (birinapant
208 with paclitaxel and birinapant with carboplatin) was further validated through clonogenic cell
209 survival in *ΔCASP8* cells (**Figure 3F**) and by co-treatment with a Caspase 8- specific inhibitor (Z-
210 IETD-FMK) (**Supplementary Figure 6D**). Paclitaxel monotherapy appeared to induce necroptotic
211 cell death, as indicated by the increased resistance to paclitaxel observed in Δ*RIPK3* OVCAR3
212 cells (**Figure 3E**). Taken together, these results indicate that treatment of either paclitaxel or
213 carboplatin simultaneously with birinapant primarily induces cell death through Caspase 8-
214 mediated apoptosis. Furthermore, the results also suggest that activation of the NF-κB pathway,
215 whether through the non-canonical or canonical pathways, may modulate cellular responses to
216 the applied treatment.
217
218 **TNFα pathway activation triggered by tumor-associated macrophages enhances cancer**
219 **cell apoptosis**
220 Despite initially responding to chemotherapy, 20% of HGSOC patients relapse within 6 months
221 after completing primary chemotherapy treatment, while 60% of the patients relapse after 6
222 months *(50)*. Patients who relapse after a treatment-free interval of more than six months often
223 receive additional carboplatin or paclitaxel-based chemotherapy *(51)*. However, multiple

224 recurrences increase the likelihood of developing platinum resistance, consequently resulting in
225 poor survival *(52, 53)*.
226 To evaluate the potential of our bimodal treatment in enhancing chemotherapy effectiveness for
227 patients with multiple relapses, we analyzed viable HGSOC cells derived from longitudinal
228 samples collected at two disease recurrences (**Figure 4A**). Ascites taken at the time of the first
229 and second relapse were subjected to *ex vivo* drug testing for carboplatin, birinapant, carboplatin
230 with paclitaxel, and bimodal treatments. Overall, bimodal treatments revealed the highest efficacy
231 in inducing tumor cell-specific apoptosis (E-Cadherin^{+}, cCASP3^{+}) compared to the remaining
232 treatments tested (**Figure 4B and C**). Interestingly, bimodal treatments were generally more
233 effective in reducing tumor cell viability at the second relapse time point compared to the first
234 relapse.
235 In the complex ecosystem of tumor tissues, it is well-described that the tumor and the surrounding
236 cells within the TME may be active participants in both the production and response to TNFα
237 cytokine *(54, 55)*. Considering the pivotal role of TNFα in the apoptosis- mediated drug synergies
238 for our bimodal treatments, we performed an integrated analysis on samples derived from the
239 Swiss Tumor Profiler *(56)*. This analysis aimed to shed light on the potential contribution of
240 different cell types within the TME to TNFα signaling activation and treatment response. This
241 investigation included bulk RNA sequencing, cytometry by time-of-flight (CyTOF), and imaging
242 mass cytometry (IMC) from the same sampling sites, obtained from patients with HGSOC who
243 underwent neoadjuvant treatment. Based on our prior findings, we hypothesized that these
244 patient samples were enriched in TNFα production post-neoadjuvant chemotherapy
245 (**Supplementary Figure 5D**). Results from this analysis revealed a very strong positive
246 correlation (spearman rho= 0.93, p=*0.007*, FDR=0.0317) between the TNFα gene sets and the
247 fraction of tumor-associated macrophages (TAMs) (**Figure 4D-H, and Supplementary Figure**
248 **7**). To explore deeper into the IMC findings on the correlation between TAMs and TNFα gene
249 sets, we conducted a deconvolution analysis of matching bulk RNA sequencing focusing on the
250 immune compartment using CIBERSORT for relative quantification of the immune compartment
251 using LM22 signature matrix *(57)*. Our analysis revealed an enrichment of myeloid cells
252 (monocytes and M2 macrophages) in samples exhibiting increased activation of TNFα gene sets
253 (**Figure 5A**).
254 These findings prompted us to examine the impact of macrophage on responses to bimodal
255 treatments in *ex vivo* cultures of longitudinal samples. Analysis of the percentage of macrophages
256 (CD68^{+}) across these samples revealed a higher CD68^{+} cell fraction in the second relapse,
257 aligning with an enhanced cellular response to bimodal treatments compared to the first relapse
258 (**Figure 4C and Figure 5B**). Additionally, supplementing *ex vivo* cultures with TNFα could further
259 enhance the efficiency of the bimodal treatments (**Figure 5C and D**). In summary, these findings

260 suggest a potential role for TAMs as a predictive biomarker for the response to bimodal treatments
261 by regulating the TNFα pathway activation.

262 **Discussion**

263 HGSOC is recognized as an extremely heterogeneous disease, presenting unique treatment
264 challenges. Emerging therapeutic approaches aim to enhance patient outcomes by precisely
265 identifying patient subgroups that will ultimately benefit from the applied treatment. The
266 identification of such groups is based on multiple features of each tumor, including TME
267 composition, genetic, and molecular profiles. Our approach seeks to improve patient stratification
268 while maximizing the effectiveness of novel therapeutic approaches, thereby enhancing the
269 quality of life and prolonging progression and disease-free survival. In this study, we introduce a
270 novel approach to enhance the effectiveness of chemotherapy in HGSOC through co-treatment
271 with SMAC mimetics. Our findings demonstrate that SMAC mimetics, particularly birinapant, in
272 combination with either carboplatin or paclitaxel, trigger a Caspase 8-dependent apoptotic
273 program facilitated by increased TNFα production and signaling activation. Through our analysis
274 of neoadjuvant-treated HGSOC samples, we identified a positive correlation between TAMs and
275 TNFα-related gene sets. Moreover, our experiments with HGSOC *ex vivo* cultures revealed a
276 significant association between high TAM abundance and enhanced responses to the bimodal
277 treatments. This suggests a potential role for TAMs in modulating drug responses through the
278 mediation of TNFα signaling, highlighting their potential utility as predictive biomarkers for the
279 proposed bimodal treatments.

280 Our study has uncovered a promising avenue in targeted therapy in combination with
281 chemotherapy for HGSOC. Specifically, we have identified SMAC mimetics as a class of drugs
282 that exhibit a preferential affinity for EOC cells exhibiting low MSLN expression. Additionally, our
283 investigation has unveiled a compelling synergy between SMAC mimetics and standard
284 chemotherapeutic agents with the potential to enhance the efficacy of treatment regimens in
285 HGSOC patients. Notably, our results highlight the remarkable increases in TNFα expression
286 following exposure to first-line chemotherapy. This, combined with validation experiments,
287 indicates that TNFα acts as a driving force behind the observed synergies. Furthermore, we
288 hypothesize that the reduction in MSLN protein levels in EOC cells, after exposure to carboplatin
289 or paclitaxel chemotherapy, enhances cell death triggered by increased TNFα production in the
290 presence of SMAC mimetics. This hypothesis is supported by a previous report showing
291 increased resistance to TNFα-induced cell death in MSLN-expressing cancer cells *(11)*.

292 While the exact mechanism through which MSLN contributes to heightened resistance to TNFα-
293 induced cell death remains incomplete, previous studies have suggested that MSLN induces the
294 activation of the NF-κB pathway, resulting in the overexpression of multiple anti-apoptotic factors
295 *(11, 58–60)*, thereby contributing to increased resistance to TNFα-induced cell death *(11)*. These
296 findings align with data presented in the current study, where *MSLN* knockout cancer cells
297 displayed enhanced sensitivity to TNFα, birinapant, and the combination of birinapant with
298 paclitaxel. It is worth noting that, in contrast to TNFα, the supplementation with IFNγ did not result

299 in increased activation of Caspase 3 and 8 after exposure to birinapant or bimodal treatments.
300 However, previous studies reported that IFNγ supplementation increases caspase activity
301 following exposure to SMAC mimetics (BV6) in breast and colon cell line cancer models *(46)*.
302 These differences between our results and the literature may suggest a cancer model-dependent
303 effect of the combination of cytokines with SMAC mimetics, or dependent on the SMAC mimetic
304 applied, considering their documented varying effects on target proteins *(39)*. Additionally, as
305 recently reported by Cremona *et al.*, the genetic background of cancer models can influence the
306 response to SMAC mimetics. This influence was demonstrated recently by the enhanced
307 response to SMAC mimetics in *BRCA1* mutant cells as compared with *BRCA* wild-type cells *(61)*.
308 Therefore, further investigation is necessary to elucidate the role of different inflammatory
309 cytokines on the activation of different programs of PCD in combination with SMAC mimetics
310 across various cancer models.
311 SMAC mimetics have been reported to activate both apoptosis and necroptosis, two distinct
312 pathways of PCD *(43)*. The pharmacological induction of necroptosis is considered a promising
313 approach to overcome apoptosis evasion of tumor cells *(41, 62, 63)*. However, necroptosis has a
314 dual role in cancer, it can either promote or inhibit tumor growth, depending on the specific cancer
315 type and context. As a fail-safe mechanism of PCD, necroptosis can prevent tumor growth in
316 cases where apoptosis induction fails. Nonetheless, as a form of necrotic cell death, necroptosis
317 can trigger inflammatory responses and reportedly promote cancer metastasis and
318 immunosuppression *(64, 65)*. In our present study, we demonstrated that the combination of the
319 birinapant with either carboplatin or paclitaxel chemotherapy primarily induces cell death through
320 Caspase-8-mediated apoptosis. These findings are inconsistent with a previous study that
321 reported SMAC mimetics to enhance the antitumor effect of carboplatin combined with paclitaxel
322 in ovarian cancer models through a Caspase 8- independent mechanism *(66)*. In this work, the
323 effect on cell death was reported in cells with Caspase 8 knockdown when a triple combination
324 of birinapant, paclitaxel, and carboplatin was applied. However, when tested individually,
325 birinapant exhibited synergy with paclitaxel but an antagonism effect with carboplatin in caspase
326 8-depleted cells *(66)*. While we cannot dismiss that the inconsistencies between our results and
327 the previous report might arise from different measurements and experimental setups, a possible
328 explanation could relate to the use of a triple combination (birinapant, carboplatin, and paclitaxel).
329 Of note, one of the two cell line models used, OVCAR8, has been reported to exhibit resistance
330 to NF-κB inhibition *(67)*, indicating reduced responsiveness to TNFα signaling. Interestingly,
331 Hernandez *et al.* also noted an increase in cell death for the combination of birinapant with either
332 paclitaxel or carboplatin in Caspase 8 expressing models. While further investigations are
333 necessary, these results imply marginal advantages in utilizing a triple combination of birinapant,
334 carboplatin, and paclitaxel compared to the bimodal treatments.

The TME has been reported to influence tumor evolution by altering the milieu of growth factors and cytokines following chemotherapy *(68–70)*. Changes in cytokine levels produced by stromal cells after chemotherapy tend to favor cancer cells expressing the corresponding receptors *(71)*. In the current study, we found a compelling positive correlation between the presence of TAMs and the activation of TNFα gene sets in neoadjuvant-treated HGSOC samples. Among the various cell types in the TME, macrophages are recognized as the major contributor to TNFα production and signaling activation *(72, 73)*, which supports the findings of in the current study. Additional studies are required to fully understand the interaction and contribution of various cell types, especially TAMs, in the TME and their influence on TNFα signaling in tumor cells. This is particularly relevant in the context of the bimodal treatment where the synergistic effect of SMAC mimetics in combination with either carboplatin or paclitaxel depends on the TNFa signaling. By mechanistically unraveling the interplay between MSLN expression, TNFα signaling, TAMs, and the enhanced efficacy of bimodal treatments, we provide valuable insights that may guide the application of these therapeutic approaches in patients with recurrent HGSOC. While further research is needed to explore how different cell types in the TME contribute to TNFα signaling in tumor cells and the effects of combination therapies, our study established the groundwork for an exciting avenue in the treatment of this challenging disease. Specifically, our results suggest that TAMs enriched in the TME could potentially act as biomarkers for the proposed bimodal treatment, assisting in better patient stratification. Overall, our findings hold promise in improving patient outcomes, especially for those dealing with recurrent HGSOC.

355 **Material and methods**

356 **Patient-derived cells**

357 All HGSOC patient-derived samples and associated data included in this study fully adhere to
358 ethical standards. Ethical approval was granted by the Ethical Committee of Northwest and
359 Central, Switzerland (EKNZ, BASEC IDs: 2017-01900 and 2023-00988). All patients' clinical
360 characteristics are provided in **Supplementary Table 2**.

361

362 **Human cell lines**

363 Ovarian cancer cell lines (Kuramochi, COV362, COV318, OVCAR3, OVCAR4, OVCAR5,
364 OVCAR8, BG1, SKOV3, SKOV3 IP, ES-2, OVSAHO, A2780, A2780 cisplatin-resistant, TYKnu,
365 TYKnu cisplatin-resistant, IGROV1, and IGROV1 paclitaxel-resistant) obtained from different
366 commercial sources (**Supplementary Table 4**) were cultured in RPMI 1640 (Sigma-Aldrich)
367 containing 10% fetal bovine serum (FBS) (Sigma-Aldrich) and 1% of penicillin/streptomycin
368 (Sigma-Aldrich). Immortalized human mesothelial cell line MeT5A (ATCC) was maintained in
369 Medium 199 (Sigma-Aldrich) containing 10% FBS, 3.3 nM epidermal growth factor (EGF)
370 (PeproTech), 400 nM hydrocortisone (Sigma-Aldrich), 870 nM Bovine insulin (Sigma-Aldrich), 20
371 nM HEPES (Sigma-Aldrich) and 1:1000 of trace elements B (Corning). All cell lines were
372 maintained at 37°C and 5% CO_2 authenticated using short tandem repeat (STR) profiling
373 (Microsynth AG) and regularly tested for the absence of mycoplasma *(74)*. To study the role of
374 MSLN in drug sensitivity and resistance we used a previously established and characterized cell
375 line models: parental ($MSLN^{high}$) and MSLN knockout (*ΔMSLN*) OVCAR8 and OVCAR3 cell lines,
376 as well as parental ($MSLN^{low}$) and MSLN overexpressing (MSLN OE- $MSLN^{high}$) BG1 and
377 OVCAR4 cells *(15)*. These EOC cell lines were initially selected based on their nature of MSLN
378 expressing levels.

379

380 **Drug sensitivity and resistance testing (DSRT)**

381 We used the DSRT system developed at the Institute for Molecular Medicine Finland (FIMM) for
382 drug library screening. The FIMM oncology library- FO
383 (https://www.helsinki.fi/en/infrastructures/drug-discovery-chemical-biology-and-
384 screening/infrastructures/high-throughput-biomedicine/chemical-compound-libraries), consists of
385 528 approved and investigational oncology drugs including target compounds such as kinase
386 inhibitors, epigenetic modifiers, differentiating agents and conventional chemotherapeutics. The
387 compounds were dispensed in 384-well plates (Corning) at five different concentrations covering
388 1 and 10000nM range, using acoustic liquid dispensing technology (Echo 550; Labcyte Inc.).
389 Assay-ready plates were stored in pressurized StoragePods (Roylan Developments) under an
390 inert atmosphere until used. Before DSRT, growth patterns, and rates were evaluated by viability
391 assays to ensure logarithmic cell growth during the 72 hours of drug exposure. Using a

392 MultiDrop™ Combi dispenser (Thermo Fisher Scientific) 5µL of culture media (RPMI 1640
393 supplemented with 10% FBS and 1% Pen/strep) was dispensed into assay-ready plates followed
394 by a brief centrifugation. Next, ovarian cancer cells (OVCAR3, OVCAR8, BG1, and OVCAR4)
395 and mesothelial cells, MeT5A, were seeded at the density of 1.5 to $2x10^3$ cells/well in 20µl of
396 media using the Multidrop Combi dispenser (Thermo Fisher Scientific) into drug-containing plates
397 followed by brief centrifugation and incubated for 72 hours at 37°C in the presence of 5% CO_2.
398 Cell viability/cellular ATP levels were measured with CellTiter-Glo 2.0 (CTG, Promega) with
399 detection on the Ensight plate reader (PerkinElmer). Raw data were further processed to calculate
400 the drug efficacies of individual drugs. Using in-house software, data from the plate reader were
401 normalized per plate to the percent of cell viability in control wells (DMSO, and benzethonium
402 chloride- BzCl). Concentration-response curves were fitted to percent viability values using a four-
403 parameter logistic model and processed further to a sensitivity metric (drug sensitivity score; DSS)
404 using a weighted area-under-the-curve calculation *(75)*. For the validation experiments, hit
405 compounds and controls (DMSO, 100 µM BzCl) were pre-dispensed on 384-well plates (Corning)
406 using the Echo 550 (Labcyte Inc). Each compound was plated as quadruplicate in eight
407 concentrations (3-fold dilution).
408
409 **Dose-response matrix analysis and synergy scoring**
410 For the synergy experiments, we used 384-well screening plates with five concentrations per
411 compound in duplicate (carboplatin in combination with paclitaxel) or triplicate (birinapant,
412 LCL161 in combination either with carboplatin or paclitaxel, all dissolved in the same solution).
413 Cell seeding, viability, and calculation of DSS values (for cell lines and patient-derived samples,
414 **Supplementary Table 2**) were performed as described above for DSRT. Response matrices
415 were then calculated using the ZIP reference model with the SynergyFinder web application
416 (version 3.0; synergyfinder.fimm.fi) *(34)*. Combinations with a score > 10 were considered to
417 exhibit a strong synergy and <-10 a strong antagonism. Scores between 5 and 10 were
418 considered moderately synergistic, between -5 to -10 as moderately antagonistic, and between -
419 5 and 5 were indicative of additive effects.
420
421 **Evaluation of drug efficiency using live cell confocal microscopy**
422 Parental and Δ*MSLN* OVCAR3 cells were manually seeded into 384-well CellCarrier culture
423 plates (PerkinElmer) at the density of $2x10^3$ cells/well in 20µl of media (RPMI 1640 supplemented
424 with 10% FBS and 1% Pen/strep) and incubated for 24 hours. For the co-culture assay, equal
425 amounts of each cell population (1000 cells/well) were seeded in 20µl of media. After the
426 incubation time, 5µl of POPO™-1 Iodide (Thermo Scientific) diluted in culture media (final
427 concentration of 0.2µM) was added to all the wells of the plate. Birinapant (4000nM to 1.8nM
428 concentration) was added in 5µl of media to the wells in quadruplicate as well as a negative

429 (DMSO 0.1%) and positive control (BzCl 100µM) followed by time-lapse microscopy using the
430 OperaPhenix microscope (PerkinElmer) for 48 hours. Image acquisition and quantification of
431 POPO™-1 iodide staining intensity were done using the Harmony high-content imaging and
432 analysis software 4.8 (PerkinElmer). Mesothelial clearance was performed by seeding MeT5A-
433 GFP cells *(15)* at the density of 1.3x 10^4 cells/well into 384-well CellCarrier plates (PerkinElmer),
434 pre-coated with 10µg/ml collagen type I (Sigma-Aldrich), in 20µl of media. In parallel, ovarian
435 cancer cell aggregates were generated by seeding the cells into t25 micro cavity flasks (Corning)
436 followed by a 24-hour incubation. After incubating, aggregates (10µl ~7 aggregates) were
437 transferred to the plate containing the MeT5A-EGFP cells and exposed to a gradient
438 concentration of birinapant (4000nM to 1.8nM). POPO™-1 Iodide death marker (Thermo Fisher
439 Scientific) was added to all the wells of the plate at the final concentration of 0.2µM followed by
440 24-hour time-lapse microscopy using the OperaPhenix microscope (PerkinElmer). Image
441 acquisition and quantification of POPO™-1 Iodide (Thermo Fisher Scientific) staining intensity
442 was done using the Harmony high-content imaging and analysis software 4.8 (PerkinElmer).
443
444 **Immunoblotting**
445 EOC cell lines were lysed in 1x radioimmunoprecipitation assay buffer (RIPA, Cell Signaling
446 Technology, BioConcept) containing a proteinase inhibitor cocktail (Sigma-Aldrich). Lysates were
447 clarified by centrifugation at 18,000 g for 15 minutes at 4°C. Clarified lysates were quantified using
448 the Pierce TM BCA protein assay (Promega) and boiled in 1x sample buffer (50 mM Tris-HCl, 1%
449 SDS, 100 mM DTT, and 10% glycerol) at 95°C for 5 min and resolved by SDS-PAGE. Proteins
450 were then transferred to a polyvinylidene difluoride (PVDF) membrane (BioRad) and blocked with
451 5% (w/v) bovine serum albumin in TBS-T (20 mM Tris-Base, 150 mM NaCl, pH 7.8, 0.1% Tween
452 20) for 1 hour at room temperature. The membrane was incubated with one of the listed primary
453 antibodies (**Supplementary Table 5**) diluted in 5 % (w/v) BSA in TBS-T overnight at 4°C. After
454 washing (3 times, 10 minutes) in TBS-T, membranes were incubated with corresponding HRP-
455 conjugated secondary antibodies (1:10000, Cell Signaling, BioConcept) for 3 hours at room
456 temperature. Finally, the membrane was incubated with Super Signal West Dura Extended
457 Duration Substrate (Thermo Fisher Scientific) for the detection of the HRP signal. Western blot
458 results were visualized by Gel Doc XR+TM (BioRad) and analyzed by Image Lab™ software
459 (BioRad). Original membrane images can be found in the **Supplementary Figure 8-12**.
460
461 ***Ex vivo* patient-derived cultures**
462 Tissue or ascites samples were thawed (retrospective cohort), and digested into single cells
463 (tissues) using a mix of collagenase/dispase (Roche), accutase (Millipore), DNAse type IV (New
464 England Biolabs/ Bioconcept) in DMEM/F12 (Sigma-Aldrich) for 1 hour at 37°C under agitation.
465 After digestion, samples were filtered through a 70µm cell strainer and washed with PBS (Sigma-

466 Aldrich). Cells were then seeded into agarose chips, which were pre-made using MicroTissues
467 3D petri dish micro-mold (Sigma-Aldrich), at a density of $2.5x10^5$ cells/ chip in 200µl of Ovarian
468 TumorMACS™ (Miltenyi Biotec) medium and incubated for 24 hours. Patient-derived cells were
469 then exposed to the different drugs and their combinations for 48 hours followed by fixation with
470 4% formalin (Formafix AG) for 20 minutes at room temperature. After fixation cells were washed
471 with PBS, and to prevent cell loss in the subsequent steps, a thin layer of liquid histogel (Epredia)
472 was added to the top of the cells. Agarose chips were then subjected to a standard paraffin
473 embedding protocol and sectioned at 5µm thickness followed by immunofluorescence staining.
474
475 **Immunofluorescence**
476 After deparaffinization, heat-induced (98°C) antigen retrieval was performed with a citrate buffer
477 (pH 6.0) (Thermo Fisher Scientific), and slides were incubated with Triton X-100 0.25% in PBS
478 for 5 minutes, washed in PBS for another 5 minutes followed by incubation with blocking solution
479 (5% FBS with 1% BSA in PBS 1% Triton-X 100) for 1 hour. After blocking, samples were
480 incubated with one of the listed primary antibodies (**Supplementary Table 5**) diluted in 1% BSA
481 0.1% Triton-X 100 in PBS and incubated overnight at 4°C. Primary antibodies were detected
482 using goat anti-mouse or anti-rabbit IgG (H+L) Alexa fluor 488 or 647 (Cell signaling
483 Technologies/ Bioconcept) secondary antibodies diluted 1:500 in 1% BSA 0.1% Triton-X 100 in
484 PBS for 3 hours in the dark at room temperature. Slides were mounted using ProLong® Gold
485 antifade reagent (Cell Signaling Technology, BioConcept) and a coverslip. Images were taken
486 using the confocal microscope Nikon CSU-W1, analyzed with Image J (2.3.0/1.53q) and Qupath
487 (0.3.0) software, and developed scripts for cell detection and annotations. Further analyses were
488 performed by R/Bioconductor.
489
490 **Zebrafish embryo tumor xenograft**
491 All zebrafish experiments and husbandry followed federal guidelines complied with the Swiss
492 Animal Protection Ordinance and were approved by the Cantonal Veterinary Commission of
493 Basel-Stadt. The xenotransplantation experiments were performed as previously described with
494 minor alterations *(35, 76)*. Zebrafish embryos were anesthetized in 0.02% tricaine (Sigma-Aldrich)
495 at 2- day post fertilization (dpf) and 250–350 COV362 cells (stable expressing dTomato
496 fluorescent protein) were microinjected into the vessel-free area of the yolk of a transgenic
497 Tg(*kdrl:eGFP*) line. Embryos harboring cells were incubated at 35°C in 1x E3 medium containing
498 either DMSO 0.1% or birinapant in combination with paclitaxel at the final concentration of
499 5000nM and 1000nM, respectively. Three days after transplantation, zebrafish larvae (8-9 per
500 condition) were dissociated into single cells by applying enzymatic digestion using 5µl of liberase
501 (Sigma-Aldrich) (2.5mg/ml) in a final volume of 50µl in PBS and incubated for 15 minutes at 32°C
502 with agitation 800 rpm. This incubation step was repeated three times with repeated vigorous

503 pipetting in between resulting in a total digestion time of 60 minutes. After complete digestion,
504 Liberase was inactivated by adding 5µl of 5% BSA in PBS. An additional 150 µl of PBS was
505 added, followed by filtration through a 70µm filter. The filter was rinsed once with PBS to collect
506 all cells. Single cells were washed twice with PBS and then stained with a DAPI (Biolegend)
507 solution (0.2 µg/ml) and analyzed on a CytoFLEX S (Beckman Coulter) for DAPI-negative and
508 dTomato-positive cells. The normalization for the input was performed by dividing the number of
509 dTomato$^+$ cells by the number of eGFP$^+$ (zebrafish) cells.
510 Toxicity tests of the various compounds and combinations were performed in zebrafish embryos
511 with a modified protocol based on the previously described methods *(77, 78)*. Zebrafish embryos
512 (at 2 dpf) were incubated for 3 days at 35°C in 1x E3 medium containing a gradient concentration
513 of DMSO, paclitaxel, birinapant, and birinapant in combination with paclitaxel. After the incubation
514 period, the mortality rate and general behavior were macroscopically evaluated (n=2 wells per
515 condition, each with 5 larvae). At least two larvae per condition were selected for microscopic
516 assessment of the morphology using confocal microscopy (Nikon CSU-W1). This evaluation
517 included a detailed analysis of malformation, absence of organs, or signs of organ dysfunction.
518
519 **Lentivirus production and transduction**
520 Lentivirus production was performed using the HEK29T cells that were cultured in RPMI 1640
521 with 10% FBS and 1% penicillin/streptomycin. One day before transfection 4x10^6 cells were
522 seeded into a 75cm^2 tissue culture flask. For each flask, 4µg of the plasmid encoding the targeted
523 information, pUltra (Addgene #24129), pUltra-Chili (Addgene #48687), LentiV-Cas9-puro
524 (Addgene #108100), LGR2.1 (Addgene #108098) encoding the gRNA targeting the gene of
525 interest, pLenti-CMV-Blast-FLIP-GFP-DEVD, and pLenti-CMV-Blast-FLIP-GFP-XEXD, and 2µg
526 of packaging (pCMVR8.74, Addgene #22036) and envelope (pMD2.G Addgene #12259)
527 plasmids were transfected using 24µl of jetPEI reagent and 1 ml of 150mM NaCl solution
528 (Polyplus-transfection). Culture media was changed 24 hours after transfection. The supernatant
529 containing active lentivirus particles was collected 48 hours later, filtered with a 0.45µm filter
530 (Sartorius), and stored at -80°C. Target cell lines were then transduced with the desired lentiviral
531 supernatant. If needed after 3 passages, cells were enriched for dTomato, EGFP, or mCherry
532 positive cells using the BD FACS Aria Cell sorter (BD Bioscience).
533
534 **Generation of caspase 3 and caspase 8 reporters**
535 Plasmid encoding the sequence of the cleavage site for Caspase 3 (DEVD) and FLIP-GFP
536 reporter (Addgene# 124428) was digested using the *NheI*_HF and *XmaI* (New England Biolabs,
537 Bioconcept) and cloned into the pLenti_CMV_GFP_Blast (Addgene #17445) backbone, that has
538 been previously digested with *XbaI* (New England Biolabs, Bioconcept) and *XmaI*, followed by
539 transformation into *Stbl3 E. coli* strain. The right insertion and sequence of FLIP_GFP_DEVD in

540 the pLenti_CMV_GFP_Blast backbone (pLenti_CMV_GFP_Blast_FLIP_GFP_DEVD) was
541 confirmed by Sanger DNA sequence (Microsynth) using the CMV-F primer (**Supplementary**
542 **table 6**). Caspase 8 reporter was established by replacing the DEVD amino acid sequence with
543 XEXD in pLenti_CMV_GFP_Blast_FLIP_GFP_DEVD plasmid through the In-fusion Snap
544 assembly master mix (Takara Bio) using the following oligos forward: 5'-
545 GTCTGGAAACCGATGGTGGCGGTGGCAAGGTG-3' and reverse 5-
546 CATCGGTTTCCAGACCTGATGCATCGGTAATGCCAG-3', PCR reaction was conducted under
547 the following conditions: denaturation at 98°C for 10 seconds, followed annealing at 55°C for 5
548 seconds and 72°C for 50 seconds, repeated for a total of 35 cycles. The resulting PCR product
549 was then purified using the Macherey-Nagel NucleoSpin gel and PCR clean-up kit (Thermo Fisher
550 Scientific). Linearized vector (67.4ng) was then mixed with 5X In-Fusion Snap Assembly Master
551 Mix and nuclease-free water in a final volume of 10ul. This mixture was incubated at 50°C for 15
552 minutes followed by transformation into Stellar™ competent cells a *HST08 E.coli* strain. The
553 protein-encoding XEXD DNA sequence was confirmed by the Sanger DNA sequence using the
554 CMV_F primer (**Supplementary Table 6**).
555
556 **Caspase 3 and Caspase 8 activity analysis**
557 Caspase 3 and Caspase 8 activity was visualized by flow cytometry in BG1, COV362, COV318,
558 OVCAR4, OVCAR3, and OVCAR8 cells stably expressing the FLIP-GFP reporter for caspase 3
559 and 8 activity. Cells ($5x10^4$/well) were seeded into 48-well plates and incubated for 24 hours,
560 followed by exposure to carboplatin, paclitaxel, birinapant, TNFα, IFNy, and co-treatments for 24
561 hours. Cells were then harvested and stained with DAPI (0.1µg/ml) solution. Caspase 3 and 8
562 activity ($EGFP^+$ cells) was analyzed using the CytoFLEX Flow Cytometer (Beckman Coulter) and
563 Flowjo v10 BD (Becton Dickinson) software. Caspase 3 and 8 activity was represented as the
564 percentage of $EGFP^+$ cells within the mCherry positive cells (cells with stable expression of the
565 caspase 3 or caspase 8 reporter). For each cell line, two to four independent experiments were
566 performed.
567 **Molecular cloning for the single RNAs**
568 Single guide RNAs (sgRNA) targeting protein-coding DNA sequences of target genes was
569 designed using Benchling (Biology Software, 2021, retrieved from https://benchling.com).
570 SgRNAs with high-quality scores were selected for editing of the target gene (**Supplementary**
571 **Table 7**). Single-strand oligonucleotides were purchased from Sigma-Aldrich annealed and
572 cloned into LRG2.1 (addgene, #108098) using the *BsmBI* endonuclease restriction site and
573 T4_DNA ligase (Promega) for subsequent expression of the sgRNA together with EGFP
574 fluorescent protein. Ligations were transformed into *Stbl3 E.coli* following ampicillin selection, ZR
575 Plasmid Miniprep Classic plasmid purification (ZYMO Research, Lucerna-Chem), and Sanger

576 DNA sequencing (Microsynth) to confirm insertion of respective sgRNA using the human U6
577 primer (**Supplementary Table 6**).
578
579 **CRISPR-Cas9 cell competition assay**
580 CRISPR-Cas9 cell competition assay was performed as previously described *(49)*. Stable Cas9-
581 expressing ovarian cancer cells were transduced with lentivirus particles containing sgRNAs
582 targeting selected genes (**Supplementary Table 7**). SgRNAs targeting the same gene were
583 pooled and further diluted in a 1:5 or 1:8 ratio with a complete culture growth medium. The medium
584 was changed 24 hours after transduction and cells were incubated for 2 additional days until
585 measuring the EGFP-positive cells. The percentage of fluorescence-positive cells was
586 determined initially (baseline reference, passage 0, 3 days after transduction) and all following
587 passages using the CytoFLEX Flow Cytometer (Beckman Coulter). In each passage, cells were
588 washed with FACS-wash (FW-1% FBS in PBS) in 96-well V-shape plates and stained with DAPI
589 (0.1 µg/ml) (Biolegend) for 5 minutes. All investigated cell lines were gated individually to exclude
590 debris, doublets, and dead ($DAPI^+$) cells.
591 Delivery of compounds and combinations was initiated at passage 1 and cells were kept under
592 treatment until passage 5 (20-23 days after transduction). The following concentrations were
593 used: 50 ng/ml, 1-2uM, 1-2nM, and 2-5nM of TNFα, carboplatin, paclitaxel, and birinapant.
594 Dropout values represent the fold-change of the percentage of $EGFP^+$ cells at each passage,
595 relative to passage 0, and were used as a readout of effects on cell fitness or drug sensitivity
596 conferred by the CRISPR-*Cas9* mediated gene mutations. Data analysis was performed using
597 FlowJo v10 BD (Becton Dickinson) and R/Bioconductor scripts. Relative drug sensitivity was
598 calculated by dividing the dropout values for the control condition (targeted gene without
599 treatment) by the values for the target gene under treatment.
600 Of note, due to the high number of guides applied in this study, each assay was performed at
601 least in two independent experiments with the negative control *AAVS1* (non-essential gene) and
602 at least one positive control (*RPA3* or *PCNA*). The robustness of the competition assay is
603 described in *(49)*.
604
605 **Colony formation assay**
606 Drug sensitivity was determined by the colony formation assays. OVCAR3-Cas9 cells were
607 transduced with lentivirus supernatant encoding sgRNAs targeting *AAVS1* or *CASP8*. Three
608 passages after lentivirus transduction cells were enriched for $EGFP^+$ cells using the BD FACSAria
609 Cell sorter (BD Bioscience). Cells were then seeded into 12 well plates at a density of 600
610 cells/well and exposed to the different drug combinations at the final concentration of 1µM, 1nM,
611 and 5nM for carboplatin, paclitaxel, and birinapant, respectively. Complete growth media with or
612 without drugs was replaced every 3 days. After two weeks, colonies were fixed at room

613 temperature for 1 hour and stained with 0.05% crystal violet (Sigma-Aldrich) in 4% formalin
614 (Formafix AG) the plates were then rinsed 3-4 times with water, dried, and images of the well
615 were taken using the Fusion FX7 Edge Imaging System (Witek AG).
616
617 **RT-qPCR**
618 To extract RNA, $3x10^5$ cells were seeded in 12-well plates and incubated for 48 hours. OVCAR3
619 and Kuramochi cells were then exposed to the following compounds and combinations for 24
620 hours: carboplatin (10μM), paclitaxel (10nM), birinapant (500nM), and birinapant (500nM)
621 combined with either carboplatin (10μM) or paclitaxel (10μM). Total RNA extraction was
622 performed using the RNeasy Plus universal mini kit (Qiagen). RNA was eluted in 30μl of RNase-
623 free water and the concentration was measured using a NanoDrop (Thermo Fisher Scientific). A
624 total of 1μg of RNA in 20μl reaction volume was reverse transcribed using the iScript Reverse
625 Transcription Supermix for RT-PCR (Bio-Rad). RT-qPCR was performed for *TNFA*, and reference
626 genes *SDHA* and *HSPCB (79)* in a 10μl reaction containing 25ng cDNA (initial total RNA), 400nM
627 forward and reverse primer (**Supplementary Table 6**), nuclease-free water, and 1x GoTaq
628 Master mix with ROX as a reference dye (Promega) on a Thermo ABI 7500 fast real-time PCR
629 machine (Applied Biosystem, Thermo Fisher Scientific). Quantitative PCR was performed in
630 triplicates and analyzed using the $2^{-\Delta\Delta Ct}$ method.
631
632 **TNFα supplementation and neutralization**
633 OVCAR3 and Kuramochi cells were seeded at a density of $5x10^5$ cells/ well in a 6-well plate and
634 incubated for 48 hours. Cells were then exposed for 24 hours to the following compounds and
635 combinations: carboplatin, paclitaxel, birinapant, carboplatin and birinapant, paclitaxel and
636 birinapant either supplemented with TNFα (50ng/ml, Peprotech) or with TNFα neutralizing
637 antibody (1μg/ml, Cell Signalling Technologies), following protein extraction and immunoblot
638 analysis. Rabbit IgG (Santa Cruz Technologies) was used as a non-specific binding control.
639 **Whole exome sequencing**
640 Exonic regions were captured using the Twist Biosciences Human Comprehensive Exome Panel
641 for pair-end 100bp reads, as described by the manufacturer, and sequenced on an Illumina
642 NovaSeq 6000. Post-sequencing analysis of Whole Exome Sequencing (WES) genomic data
643 included the following steps: Initially, adapter trimming was performed using SeqPurge
644 (v2022_04), retaining reads with a minimum length of 15 bp. Alignment to the reference genome
645 GRCh38 was executed with BWA MEM (v0.7.17), followed by post-processing via Samtools
646 (v1.11) and Picard (v2.27.1) for removal of PCR duplicates and secondary alignments. Base
647 recalibration was carried out using the GATK suite (v4.2.6.1).
648 Quality control metrics were assessed using the following tools: FastQC (v0.11.9), Picard, GATK,
649 Samtools, and QualiMap (v2.2.2d), with MultiQC (v1.9) for aggregating the QC results. Variant

650 calling was performed with a combination VarScan2 (v2.4.4), Mutect2 (GATK v4.2.6.1), and
651 Strelka2 (2.9.10), with variants reported by at least two of three variant callers retained for
652 downstream analyses. Variants from all samples were merged using BCFTools (v1.15.1) and
653 annotated using the Ensembl Variant Effect Predictor (VEP) (v108) with databases including
654 ClinVar, dbSNP, gnomAD, dbNSFP, and COSMIC.
655
656 **Suspension and imaging mass cytometry**
657 Cytometry by the time of flight and imaging mass cytometry experiments (CyTOF and IMC
658 respectively) were performed as described before *(80)*. For CyTOF, single cells were identified
659 using a random forest classifier trained on a subset of manually gated cells using the Cytobank
660 platform *(81)*. For IMC, cell types were identified using a series of cell clustering and random
661 forest classification steps.
662
663 **Sequencing, alignment, and counting**
664 Bulk RNA libraries were ribo-depleted and sequenced with the Illumina NovaSeq 6000 system.
665 Alignment to the reference genome (GRCh38) was performed with STAR *(82)*. The raw
666 expression counts were obtained using simple counting, an in-house pipeline accessible through
667 github:gromics (at commit #67e1f4e).
668
669 **Sample quality control**
670 Quality control of samples was performed based on their RNA Integrity Score (RIN) and the
671 following FASTQC metrics: “Per Sequence GC Content”, “Overexpressed Sequences”, “Per Base
672 Sequence Quality”, “Per Sequence Quality Scores” and “Per Base N Content”. If multiple FASTQ
673 files were generated per sample, e.g., due to sequencing separately forward and reverse reads
674 or sequencing in multiple lanes or flowcells, the FASTQC metrics were aggregated per sample,
675 with at least one FAIL/WARN resulting in FAIL/WARN for this metric for the considered sample.
676 To determine the overall sample QC, taking into account all listed FASTQC metrics as well as
677 RIN score, the following criteria were adopted: RIN below six and three or more failed FASTQC
678 modules resulted in classifying a sample as FAIL, RIN score above 7, and less than two failed
679 FASTQC modules classified samples as PASS, anything in-between or with missing information
680 categorized sample as WARN. Applying these criteria to the cohort resulted in 3 x FAIL, 11 x
681 WARN, and 38 x PASS, with both WARN and PASS samples being considered for preprocessing
682 and all downstream analyses.
683
684 **Data preprocessing**
685 Only protein-coding genes, according to Gencode release v32 (GRCh38.p13) were kept, except
686 for mitochondrial genes, and further filtered to a set of genes with more or equal to 10 counts in

687 the cohort (sum across all samples). For pathway analysis, three subsequent preprocessing steps
688 were taken: a variance stabilizing transformation (VST), batch-effect correction, and regressing
689 out effects of confounding variables. VST, which internally adjusts for differences in library sizes
690 between samples, was performed with DESeq2 *(83)*, without taking any design information into
691 account. Moreover, batch correction with remove BatchEffect from the limma package *(84)* was
692 carried out using a sequencing date as a batch (with a total of 6 batches). Furthermore, the first
693 principal component capturing differences in RIN score (Pearson's r: -0.68), as well as tumor
694 content (estimated using CyTOF data) were regressed using the remove Batch Effect function.
695
696 **Pathway activation scoring**
697 The pathway definitions, in terms of gene lists, were obtained from MSigDB (link) and KEGG (link)
698 databases, accessed on 29.07.2023. Pathway activation scores were computed using the Gene
699 Set Variation Analysis (GSVA, *(85)* with the minimum gene set size per pathway set to five,
700 Gaussian kernel, and using the normalized enrichment score (mx.diff=TRUE). The pathway
701 activation scores were then z-scored across the whole cohort, before subsetting the data to neo-
702 adjuvant cases only.
703
704 **Bulk RNA sequencing**
705 RNA-seq data was generated using the Illumina TruSeq Stranded mRNA Library Prep with 100
706 paired-end 100bp reads, according to the manufacturer's protocol, and sequenced on an Illumina
707 NovaSeq 6000. The analytical pipeline was built around the nf-core RNAseq pipeline (v3.8.1). In
708 brief, FASTQ files underwent trimming and quality control using Trim Galore (v0.6.7), and
709 Cutadapt (v.3.4) followed by mapping to the GRCh38 primary assembly using STAR (v 2.7.10a),
710 and the Gencode v41 primary annotation. Subsequent quantification was performed with Salmon
711 (v1.5.2). Quality control (QC) metrics were evaluated using featureCounts (subread v2.0.1) for
712 biotype counts, DESeq2 (v1.28.0) for Principal Component Analysis (PCA) and sample similarity,
713 Picard MarkDuplicates (v1.28.0) for identifying and marking duplicate reads, Samtools (v1.15.1)
714 for various alignment and post-alignment metrics, FastQC (v0.11.9) for basic quality metrics, and
715 RseQC (v3.0.1) for assessing RNA-seq data quality. The QC results were collated into a singular
716 report using MultiQC (v1.11). RNA-seq data were normalized using the variance stabilizing
717 transformation of the DESeq2 R (v1.36.0) package to correct for technical variances. On this data,
718 the deconvolution analysis was performed by using a Docker container pulled locally to perform
719 matrix deconvolution using the LM22 signature matrix, allowing for the quantification of relative
720 abundances in immune cells, based on the bulk expression matrix of about 600 genes provided
721 by the LM22 file.
722
723

Statistical analysis

Statistical analysis and figures were obtained using the software R Studio version 3.6.1 and 4.2 both versions were used interchangeably (www.R-project.org) and the {tidyverse} R software suite. All negative and positive controls were performed on multiple replicates at least 3 times in each cell line. All experiments were performed at least in duplicate and statistical evaluation was performed using Prism 9 software (https://www.graphpad.com/scientific-software/prism/) or R/Bioconductor. Where applicable, evaluation was done using two-way ANOVA with correction for multiple comparison tests using BH (Benjamini-Hochberg correction) or the Wilcoxon test. *p*-values of <0.05 were considered statistically significant and presented as a value or as $^{**}p < 0.01$, $^{***}p < 0.001$, $^{****}p < 0.0001$.

Acknowledgments

We are grateful to the Flow Cytometry Core Facility (Stella Stefanova and former members), Microscopy Facility (Mike Abanto, Loïc Sauteur, and Ewelina Bartoszek), Histology Facility (Diego Calabrese), Martina Konantz, Markis Affolter group (Biozentrum, University Hospital Basel, Basel, Switzerland) for their assistance and support during the zebrafish experiments, and to the Tumor Profiler consortium and Miltenyi Biotec for providing essential support and reagents.

Funding Information

The work was funded by grants Strategic Focal Area "Personalized Health and Related Technologies" grants of the ETH Domain (PHRT #2017-510 to VHS and FJ) and Krebsliga Schweiz (KFS-5389-08–2021 to FJ), Swiss National Science Foundation (#320030_207975/1 to VHS), and the Department of Biomedicine, University Hospital Basel and the University of Basel, EACR travel fellowship (5787) and EMBO short-term fellowship (8099) both to RCo. FCT project: Portuguese funds through FCT–Fundação para a Ciência e a Tecnologia/ Ministério da Ciência, Tecnologia e Inovação in the framework of the project PTDC/MEC-ONC/29503/ 2017 (to L.D.),

Author contributions

Conceptualization: RCo, FJ, LD, and BS-L
Methodology: RCo, BS-L, NR, FCL, and FJ
Investigation: RCo, SS, FCL, RL, MNL, NR, JF, RC, KBL, FS, AB, and ELML
Data curation: RCo, FCL, and FJ
Writing—original draft preparation: RCo and FJ
Writing—review, and editing: all authors read and approved the final manuscript
Visualization: RCo, FJ, FCL, RC, and JF
Supervision: LD, PO, OK, BS-L, VHS, and FJ
Project administration: LD, VHS, and FJ.

Funding acquisition: RCo, LD, VHS.

Conflict of interest

The authors declare no competing interests.

Bibliography

1. I. Tsibulak, A. G. Zeimet, C. Marth, Hopes and failures in front-line ovarian cancer therapy., *Crit. Rev. Oncol. Hematol.* **143**, 14–19 (2019).

2. R. D. Mahmood, R. D. Morgan, R. J. Edmondson, A. R. Clamp, G. C. Jayson, First-Line Management of Advanced High-Grade Serous Ovarian Cancer., *Curr. Oncol. Rep.* **22**, 64 (2020).

3. N. Colombo, J. A. Ledermann, ESMO Guidelines Committee. Electronic address: clinicalguidelines@esmo.org, Updated treatment recommendations for newly diagnosed epithelial ovarian carcinoma from the ESMO Clinical Practice Guidelines., *Ann. Oncol.* **32**, 1300–1303 (2021).

4. M. R. Mirza, R. L. Coleman, A. González-Martín, K. N. Moore, N. Colombo, I. Ray-Coquard, S. Pignata, The forefront of ovarian cancer therapy: update on PARP inhibitors., *Ann. Oncol.* **31**, 1148–1159 (2020).

5. A. Musella, C. Marchetti, M. L. Gasparri, L. Salerno, A. Casorelli, L. Domenici, L. Imperiale, I. Ruscito, T. Abdul Halim, I. Palaia, V. Di Donato, F. Pecorini, M. Monti, L. Muzii, P. B. Panici, PARP inhibition: A promising therapeutic target in ovarian cancer., *Cell Mol Biol (Noisy-le-grand)* **61**, 44–61 (2015).

6. S. N. Banerjee, C. J. Lord, First-line PARP inhibition in ovarian cancer - standard of care for all?, *Nat. Rev. Clin. Oncol.* **17**, 136–137 (2020).

7. R. Summey, D. Uyar, Ovarian cancer resistance to PARPi and platinum-containing chemotherapy., *Cancer Drug Resist.* **5**, 637–646 (2022).

8. P. Argani, C. Iacobuzio-Donahue, B. Ryu, C. Rosty, M. Goggins, R. E. Wilentz, S. R. Murugesan, S. D. Leach, E. Jaffee, C. J. Yeo, J. L. Cameron, S. E. Kern, R. H. Hruban, Mesothelin is overexpressed in the vast majority of ductal adenocarcinomas of the pancreas: identification of a new pancreatic cancer marker by serial analysis of gene expression (SAGE)., *Clin. Cancer Res.* **7**, 3862–3868 (2001).

9. K. Chang, I. Pastan, Molecular cloning of mesothelin, a differentiation antigen present on mesothelium, mesotheliomas, and ovarian cancers., *Proc Natl Acad Sci USA* **93**, 136–140 (1996).

10. H. F. Frierson, C. A. Moskaluk, S. M. Powell, H. Zhang, L. A. Cerilli, M. H. Stoler, H. Cathro, G. M. Hampton, Large-scale molecular and tissue microarray analysis of mesothelin expression in common human carcinomas., *Hum. Pathol.* **34**, 605–609 (2003).

11. U. Bharadwaj, C. Marin-Muller, M. Li, C. Chen, Q. Yao, Mesothelin confers pancreatic cancer cell resistance to TNF-α-induced apoptosis through Akt/PI3K/NF-κB activation and IL-6/Mcl-1 overexpression., *Mol. Cancer* **10**, 106 (2011).

12. U. Bharadwaj, C. Marin-Muller, M. Li, C. Chen, Q. Yao, Mesothelin overexpression promotes autocrine IL-6/sIL-6R trans-signaling to stimulate pancreatic cancer cell proliferation., *Carcinogenesis* **32**, 1013–1024 (2011).

802 13. M.-C. Chang, C.-A. Chen, P.-J. Chen, Y.-C. Chiang, Y.-L. Chen, T.-L. Mao, H.-W. Lin, W.-H.
803 Lin Chiang, W.-F. Cheng, Mesothelin enhances invasion of ovarian cancer by inducing MMP-7
804 through MAPK/ERK and JNK pathways., *Biochem. J.* **442**, 293–302 (2012).

805 14. W. F. Cheng, C. Y. Huang, M. C. Chang, Y. H. Hu, Y. C. Chiang, Y. L. Chen, C. Y. Hsieh, C.
806 A. Chen, High mesothelin correlates with chemoresistance and poor survival in epithelial ovarian
807 carcinoma., *Br. J. Cancer* **100**, 1144–1153 (2009).

808 15. R. Coelho, S. Ricardo, A. L. Amaral, Y.-L. Huang, M. Nunes, J. P. Neves, N. Mendes, M. N.
809 López, C. Bartosch, V. Ferreira, R. Portugal, J. M. Lopes, R. Almeida, V. Heinzelmann-Schwarz,
810 F. Jacob, L. David, Regulation of invasion and peritoneal dissemination of ovarian cancer by
811 mesothelin manipulation., *Oncogenesis* **9**, 61 (2020).

812 16. H. L. Kindler, S. Novello, A. Bearz, G. L. Ceresoli, J. G. J. V. Aerts, J. Spicer, P. Taylor, K.
813 Nackaerts, A. Greystoke, R. Jennens, L. Calabrò, J. A. Burgers, A. Santoro, S. Cedrés, P.
814 Serwatowski, S. Ponce, J. P. Van Meerbeeck, A. K. Nowak, G. Blumenschein, J. M. Siegel, D. A.
815 Fennell, Anetumab ravtansine versus vinorelbine in patients with relapsed, mesothelin-positive
816 malignant pleural mesothelioma (ARCS-M): a randomised, open-label phase 2 trial., *Lancet*
817 *Oncol.* **23**, 540–552 (2022).

818 17. X.-Y. Zhao, B. Subramanyam, N. Sarapa, S. Golfier, H. Dinter, Novel antibody therapeutics
819 targeting mesothelin in solid tumors., *Clin. Cancer Drugs* **3**, 76–86 (2016).

820 18. X. Liu, M. Onda, N. Watson, R. Hassan, M. Ho, T. K. Bera, J. Wei, A. Chakraborty, R. Beers,
821 Q. Zhou, A. Shajahan, P. Azadi, J. Zhan, D. Xia, I. Pastan, Highly active CAR T cells that bind to
822 a juxtamembrane region of mesothelin and are not blocked by shed mesothelin., *Proc Natl Acad*
823 *Sci USA* **119**, e2202439119 (2022).

824 19. T. Tokatlian, G. E. Asuelime, J.-Y. Mock, B. DiAndreth, S. Sharma, D. Toledo Warshaviak, M.
825 E. Daris, K. Bolanos, B. L. Luna, M. S. Naradikian, K. Deshmukh, A. E. Hamburger, A. Kamb,
826 Mesothelin-specific CAR-T cell therapy that incorporates an HLA-gated safety mechanism
827 selectively kills tumor cells., *J. Immunother. Cancer* **10** (2022), doi:10.1136/jitc-2021-003826.

828 20. K. Nagata, E. Shinto, T. Shiraishi, M. Yamadera, Y. Kajiwara, S. Mochizuki, K. Okamoto, T.
829 Einama, Y. Kishi, H. Ueno, Mesothelin Expression is Correlated with Chemoresistance in Stage
830 IV Colorectal Cancer., *Ann. Surg. Oncol.* **28**, 8579–8586 (2021).

831 21. S. Takamizawa, S. Yazaki, Y. Kojima, H. Yoshida, R. Kitadai, T. Nishikawa, T. Shimoi, K.
832 Sudo, H. S. Okuma, M. Tanioka, E. Noguchi, M. Uno, M. Ishikawa, T. Kato, Y. Fujiwara, K.
833 Yonemori, High mesothelin expression is correlated with non-squamous cell histology and poor
834 survival in cervical cancer: a retrospective study., *BMC Cancer* **22**, 1215 (2022).

835 22. Y. Li, W. Tian, H. Zhang, Z. Zhang, Q. Zhao, L. Chang, N. Lei, W. Zhang, MSLN correlates
836 with immune infiltration and chemoresistance as a prognostic biomarker in ovarian cancer., *Front.*
837 *Oncol.* **12**, 830570 (2022).

838 23. B. Yadav, T. Pemovska, A. Szwajda, E. Kulesskiy, M. Kontro, R. Karjalainen, M. M. Majumder,
839 D. Malani, A. Murumägi, J. Knowles, K. Porkka, C. Heckman, O. Kallioniemi, K. Wennerberg, T.
840 Aittokallio, Quantitative scoring of differential drug sensitivity for individually optimized anticancer
841 therapies., *Sci. Rep.* **4**, 5193 (2014).

842 24. M.-Z. Jin, W.-L. Jin, The updated landscape of tumor microenvironment and drug
843 repurposing., *Signal Transduct. Target. Ther.* **5**, 166 (2020).

844 25. J. Qian, B. L. LeSavage, K. M. Hubka, C. Ma, S. Natarajan, J. T. Eggold, Y. Xiao, K. C. Fuh,

845 V. Krishnan, A. Enejder, S. C. Heilshorn, O. Dorigo, E. B. Rankin, Cancer-associated mesothelial
846 cells promote ovarian cancer chemoresistance through paracrine osteopontin signaling., *J. Clin.*
847 *Invest.* **131** (2021), doi:10.1172/JCI146186.

848 26. H. A. Kenny, C.-Y. Chiang, E. A. White, E. M. Schryver, M. Habis, I. L. Romero, A. Ladanyi,
849 C. V. Penicka, J. George, K. Matlin, A. Montag, K. Wroblewski, S. D. Yamada, A. P. Mazar, D.
850 Bowtell, E. Lengyel, Mesothelial cells promote early ovarian cancer metastasis through fibronectin
851 secretion., *J. Clin. Invest.* **124**, 4614–4628 (2014).

852 27. M. Estermann, R. Coelho, F. Jacob, Y.-L. Huang, C.-Y. Liang, A. B. Faia-Torres, D. Septiadi,
853 B. Drasler, B. B. Karakocak, I. M. Dijkhoff, A. Petri-Fink, V. Heinzelmann-Schwarz, B. Rothen-
854 Rutishauser, A 3D multi-cellular tissue model of the human omentum to study the formation of
855 ovarian cancer metastasis., *Biomaterials* **294**, 121996 (2023).

856 28. M. Estermann, Y.-L. Huang, D. Septiadi, D. Ritz, C.-Y. Liang, F. Jacob, B. Drasler, A. Petri-
857 Fink, V. Heinzelmann-Schwarz, B. Rothen-Rutishauser, Patient-derived and artificial ascites have
858 minor effects on MeT-5A mesothelial cells and do not facilitate ovarian cancer cell adhesion.,
859 *PLoS ONE* **15**, e0241500 (2020).

860 29. P. Bouwman, J. Jonkers, The effects of deregulated DNA damage signalling on cancer
861 chemotherapy response and resistance., *Nat. Rev. Cancer* **12**, 587–598 (2012).

862 30. H. Yang, R. M. Villani, H. Wang, M. J. Simpson, M. S. Roberts, M. Tang, X. Liang, The role
863 of cellular reactive oxygen species in cancer chemotherapy., *J. Exp. Clin. Cancer Res.* **37**, 266
864 (2018).

865 31. J. H. Fine, P. Chen, A. Mesci, D. S. J. Allan, S. Gasser, D. H. Raulet, J. R. Carlyle,
866 Chemotherapy-induced genotoxic stress promotes sensitivity to natural killer cell cytotoxicity by
867 enabling missing-self recognition., *Cancer Res.* **70**, 7102–7113 (2010).

868 32. A. Koussounadis, S. P. Langdon, D. J. Harrison, V. A. Smith, Chemotherapy-induced dynamic
869 gene expression changes in vivo are prognostic in ovarian cancer., *Br. J. Cancer* **110**, 2975–2984
870 (2014).

871 33. B. Yadav, K. Wennerberg, T. Aittokallio, J. Tang, Searching for Drug Synergy in Complex
872 Dose-Response Landscapes Using an Interaction Potency Model., *Comput. Struct. Biotechnol.*
873 *J.* **13**, 504–513 (2015).

874 34. L. He, E. Kulesskiy, J. Saarela, L. Turunen, K. Wennerberg, T. Aittokallio, J. Tang, Methods
875 for High-throughput Drug Combination Screening and Synergy Scoring., *Methods Mol. Biol.* **1711**,
876 351–398 (2018).

877 35. F. Jacob, S. Alam, M. Konantz, C.-Y. Liang, R. S. Kohler, A. V. Everest-Dass, Y.-L. Huang,
878 N. Rimmer, A. Fedier, A. Schötzau, M. N. Lopez, N. H. Packer, C. Lengerke, V. Heinzelmann-
879 Schwarz, Transition of Mesenchymal and Epithelial Cancer Cells Depends on α1-4
880 Galactosyltransferase-Mediated Glycosphingolipids., *Cancer Res.* **78**, 2952–2965 (2018).

881 36. C. Cumin, Y.-L. Huang, C. Rossdam, F. Ruoff, S. P. Céspedes, C.-Y. Liang, F. C. Lombardo,
882 R. Coelho, N. Rimmer, M. Konantz, M. N. López, S. Alam, A. Schmidt, D. Calabrese, A. Fedier,
883 T. Vlajnic, M. von Itzstein, M. Templin, F. F. R. Buettner, A. Everest-Dass, F. Jacob,
884 Glycosphingolipids are mediators of cancer plasticity through independent signaling pathways.,
885 *Cell Rep.* **40**, 111181 (2022).

886 37. S. Fulda, Promises and challenges of smac mimetics as cancer therapeutics., *Clin. Cancer*
887 *Res.* **21**, 5030–5036 (2015).

888 38. E. Varfolomeev, J. W. Blankenship, S. M. Wayson, A. V. Fedorova, N. Kayagaki, P. Garg, K.
889 Zobel, J. N. Dynek, L. O. Elliott, H. J. A. Wallweber, J. A. Flygare, W. J. Fairbrother, K. Deshayes,
890 V. M. Dixit, D. Vucic, IAP antagonists induce autoubiquitination of c-IAPs, NF-kappaB activation,
891 and TNFalpha-dependent apoptosis., *Cell* **131**, 669–681 (2007).

892 39. L. Bai, D. C. Smith, S. Wang, Small-molecule SMAC mimetics as new cancer therapeutics.,
893 *Pharmacol. Ther.* **144**, 82–95 (2014).

894 40. H. Wu, J. Tschopp, S.-C. Lin, Smac mimetics and TNFalpha: a dangerous liaison?, *Cell* **131**,
895 655–658 (2007).

896 41. C. Safferthal, K. Rohde, S. Fulda, Therapeutic targeting of necroptosis by Smac mimetic
897 bypasses apoptosis resistance in acute myeloid leukemia cells., *Oncogene* **36**, 1487–1502
898 (2017).

899 42. G. Brumatti, C. Ma, N. Lalaoui, N.-Y. Nguyen, M. Navarro, M. C. Tanzer, J. Richmond, M.
900 Ghisi, J. M. Salmon, N. Silke, G. Pomilio, S. P. Glaser, E. de Valle, R. Gugasyan, M. A. Gurthridge,
901 S. M. Condon, R. W. Johnstone, R. Lock, G. Salvesen, A. Wei, J. Silke, The caspase-8 inhibitor
902 emricasan combines with the SMAC mimetic birinapant to induce necroptosis and treat acute
903 myeloid leukemia., *Sci. Transl. Med.* **8**, 339ra69 (2016).

904 43. S. McComb, J. Aguadé-Gorgorió, L. Harder, B. Marovca, G. Cario, C. Eckert, M. Schrappe,
905 M. Stanulla, A. von Stackelberg, J.-P. Bourquin, B. C. Bornhauser, Activation of concurrent
906 apoptosis and necroptosis by SMAC mimetics for the treatment of refractory and relapsed ALL.,
907 *Sci. Transl. Med.* **8**, 339ra70 (2016).

908 44. S. L. Petersen, M. Peyton, J. D. Minna, X. Wang, Overcoming cancer cell resistance to Smac
909 mimetic induced apoptosis by modulating cIAP-2 expression., *Proc Natl Acad Sci USA* **107**,
910 11936–11941 (2010).

911 45. Y. Gong, Z. Fan, G. Luo, C. Yang, Q. Huang, K. Fan, H. Cheng, K. Jin, Q. Ni, X. Yu, C. Liu,
912 The role of necroptosis in cancer biology and therapy., *Mol. Cancer* **18**, 100 (2019).

913 46. M. J. Cekay, S. Roesler, T. Frank, A.-K. Knuth, I. Eckhardt, S. Fulda, Smac mimetics and type
914 II interferon synergistically induce necroptosis in various cancer cell lines., *Cancer Lett.* **410**, 228–
915 237 (2017).

916 47. A. K. Srivastava, S. Jaganathan, L. Stephen, M. G. Hollingshead, A. Layhee, E. Damour, J.
917 P. Govindharajulu, J. Donohue, D. Esposito, J. P. Mapes, R. J. Kinders, N. Takebe, J. E.
918 Tomaszewski, S. Kummar, J. H. Doroshow, R. E. Parchment, Effect of a Smac Mimetic (TL32711,
919 Birinapant) on the Apoptotic Program and Apoptosis Biomarkers Examined with Validated
920 Multiplex Immunoassays Fit for Clinical Use., *Clin. Cancer Res.* **22**, 1000–1010 (2016).

921 48. Q. Zhang, A. Schepis, H. Huang, J. Yang, W. Ma, J. Torra, S.-Q. Zhang, L. Yang, H. Wu, S.
922 Nonell, Z. Dong, T. B. Kornberg, S. R. Coughlin, X. Shu, Designing a green fluorogenic protease
923 reporter by flipping a beta strand of GFP for imaging apoptosis in animals., *J. Am. Chem. Soc.*
924 **141**, 4526–4530 (2019).

925 49. R. Coelho, A. Tozzi, M. Disler, F. Lombardo, A. Fedier, M. N. López, F. Freuler, F. Jacob, V.
926 Heinzelmann-Schwarz, Overlapping gene dependencies for PARP inhibitors and carboplatin
927 response identified by functional CRISPR-Cas9 screening in ovarian cancer., *Cell Death Dis.* **13**,
928 909 (2022).

929 50. M. Luyckx, J.-L. Squifflet, A. M. Bruger, J.-F. Baurain, in *Ovarian Cancer*, S. Lele, Ed. (Exon
930 Publications, Brisbane (AU), 2022).

931 51. T. Baert, A. Ferrero, J. Sehouli, D. M. O'Donnell, A. González-Martín, F. Joly, J. van der
932 Velden, P. Blecharz, D. S. P. Tan, D. Querleu, N. Colombo, A. du Bois, J. A. Ledermann, The
933 systemic treatment of recurrent ovarian cancer revisited., *Ann. Oncol.* **32**, 710–725 (2021).

934 52. P. G. Rose, Ovarian cancer recurrence: is the definition of platinum sensitivity modified by
935 PARPi, bevacizumab or other intervening treatments? : a clinical perspective., *Cancer Drug*
936 *Resist.* **5**, 415–423 (2022).

937 53. S. Pignata, S. C Cecere, A. Du Bois, P. Harter, F. Heitz, Treatment of recurrent ovarian
938 cancer., *Ann. Oncol.* **28**, viii51–viii56 (2017).

939 54. E. Dondossola, A. S. Dobroff, S. Marchiò, M. Cardó-Vila, H. Hosoya, S. K. Libutti, A. Corti, R.
940 L. Sidman, W. Arap, R. Pasqualini, Self-targeting of TNF-releasing cancer cells in preclinical
941 models of primary and metastatic tumors., *Proc Natl Acad Sci USA* **113**, 2223–2228 (2016).

942 55. H. Zhao, L. Wu, G. Yan, Y. Chen, M. Zhou, Y. Wu, Y. Li, Inflammation and tumor progression:
943 signaling pathways and targeted intervention., *Signal Transduct. Target. Ther.* **6**, 263 (2021).

944 56. A. Irmisch, X. Bonilla, S. Chevrier, K.-V. Lehmann, F. Singer, N. C. Toussaint, C. Esposito, J.
945 Mena, E. S. Milani, R. Casanova, D. J. Stekhoven, R. Wegmann, F. Jacob, B. Sobottka, S.
946 Goetze, J. Kuipers, J. Sarabia Del Castillo, M. Prummer, M. A. Tuncel, U. Menzel, M. P.
947 Levesque, The Tumor Profiler Study: integrated, multi-omic, functional tumor profiling for clinical
948 decision support., *Cancer Cell* **39**, 288–293 (2021).

949 57. A. M. Newman, C. L. Liu, M. R. Green, A. J. Gentles, W. Feng, Y. Xu, C. D. Hoang, M. Diehn,
950 A. A. Alizadeh, Robust enumeration of cell subsets from tissue expression profiles., *Nat. Methods*
951 **12**, 453–457 (2015).

952 58. C. Marin-Muller, D. Li, U. Bharadwaj, M. Li, C. Chen, S. E. Hodges, W. E. Fisher, Q. Mo, M.-
953 C. Hung, Q. Yao, A tumorigenic factor interactome connected through tumor suppressor
954 microRNA-198 in human pancreatic cancer., *Clin. Cancer Res.* **19**, 5901–5913 (2013).

955 59. M.-C. Chang, C.-A. Chen, C.-Y. Hsieh, C.-N. Lee, Y.-N. Su, Y.-H. Hu, W.-F. Cheng,
956 Mesothelin inhibits paclitaxel-induced apoptosis through the PI3K pathway., *Biochem. J.* **424**,
957 449–458 (2009).

958 60. Z. Tang, M. Qian, M. Ho, The role of mesothelin in tumor progression and targeted therapy.,
959 *Anticancer Agents Med Chem* **13**, 276–280 (2013).

960 61. M. Cremona, C. J. Vandenberg, A. M. Farrelly, S. F. Madden, C. Morgan, R. Kalachand, J. N.
961 McAlpine, S. Toomey, D. G. Huntsman, L. Grogan, O. Breathnach, P. Morris, M. S. Carey, C. L.
962 Scott, B. T. Hennessy, BRCA mutations lead to XIAP overexpression and sensitise ovarian
963 cancer to inhibitor of apoptosis (IAP) family inhibitors., *Br. J. Cancer* **127**, 488–499 (2022).

964 62. Z. Su, Z. Yang, L. Xie, J. P. DeWitt, Y. Chen, Cancer therapy in the necroptosis era., *Cell*
965 *Death Differ.* **23**, 748–756 (2016).

966 63. S. Hannes, R. Karlowitz, S. J. L. van Wijk, The Smac mimetic BV6 cooperates with STING to
967 induce necroptosis in apoptosis-resistant pancreatic carcinoma cells., *Cell Death Dis.* **12**, 816
968 (2021).

969 64. L. Seifert, G. Werba, S. Tiwari, N. N. Giao Ly, S. Alothman, D. Alqunaibit, A. Avanzi, R. Barilla,
970 D. Daley, S. H. Greco, A. Torres-Hernandez, M. Pergamo, A. Ochi, C. P. Zambirinis, M. Pansari,
971 M. Rendon, D. Tippens, M. Hundeyin, V. R. Mani, C. Hajdu, G. Miller, The necrosome promotes
972 pancreatic oncogenesis via CXCL1 and Mincle-induced immune suppression., *Nature* **532**, 245–
973 249 (2016).

974 65. B. Strilic, L. Yang, J. Albarrán-Juárez, L. Wachsmuth, K. Han, U. C. Müller, M. Pasparakis, S.
975 Offermanns, Tumour-cell-induced endothelial cell necroptosis via death receptor 6 promotes
976 metastasis., *Nature* **536**, 215–218 (2016).

977 66. L. F. Hernandez, A. B. Dull, S. Korrapati, C. M. Annunziata, Smac-mimetic enhances
978 antitumor effect of standard chemotherapy in ovarian cancer models via Caspase 8-independent
979 mechanism., *Cell Death Discov.* **7**, 134 (2021).

980 67. L. Hernandez, M. K. Kim, A. M. Noonan, E. Sagher, H. Kohlhammer, G. Wright, L. T. Lyle, P.
981 S. Steeg, M. Anver, D. D. Bowtell, Australian Ovarian Cancer Study Group 57, C. M. Annunziata,
982 A dual role for Caspase8 and NF-κB interactions in regulating apoptosis and necroptosis of
983 ovarian cancer, with correlation to patient survival., *Cell Death Discov.* **1**, 15053 (2015).

984 68. L. R. Sanchez, L. Borriello, D. Entenberg, J. S. Condeelis, M. H. Oktay, G. S. Karagiannis,
985 The emerging roles of macrophages in cancer metastasis and response to chemotherapy., *J.*
986 *Leukoc. Biol.* **106**, 259–274 (2019).

987 69. D. W. Edwardson, A. M. Parissenti, A. T. Kovala, Chemotherapy and Inflammatory Cytokine
988 Signalling in Cancer Cells and the Tumour Microenvironment., *Adv. Exp. Med. Biol.* **1152**, 173–
989 215 (2019).

990 70. R. Hughes, B.-Z. Qian, C. Rowan, M. Muthana, I. Keklikoglou, O. C. Olson, S. Tazzyman, S.
991 Danson, C. Addison, M. Clemons, A. M. Gonzalez-Angulo, J. A. Joyce, M. De Palma, J. W.
992 Pollard, C. E. Lewis, Perivascular M2 Macrophages Stimulate Tumor Relapse after
993 Chemotherapy., *Cancer Res.* **75**, 3479–3491 (2015).

994 71. E. Hirata, E. Sahai, Tumor microenvironment and differential responses to therapy., *Cold*
995 *Spring Harb. Perspect. Med.* **7** (2017), doi:10.1101/cshperspect.a026781.

996 72. F. Balkwill, Tumour necrosis factor and cancer., *Nat. Rev. Cancer* **9**, 361–371 (2009).

997 73. B.-Z. Qian, J. W. Pollard, Macrophage diversity enhances tumor progression and metastasis.,
998 *Cell* **141**, 39–51 (2010).

999 74. C. C. Uphoff, H. G. Drexler, Detection of mycoplasma contaminations., *Methods Mol. Biol.*
1000 **290**, 13–23 (2005).

1001 75. S. Potdar, F. Ianevski, A. Ianevski, Z. Tanoli, K. Wennerberg, B. Seashore-Ludlow, O.
1002 Kallioniemi, P. Östling, T. Aittokallio, J. Saarela, Breeze 2.0: an interactive web-tool for visual
1003 analysis and comparison of drug response data., *Nucleic Acids Res.* **51**, W57–W61 (2023).

1004 76. Y.-L. Huang, C.-Y. Liang, D. Ritz, R. Coelho, D. Septiadi, M. Estermann, C. Cumin, N.
1005 Rimmer, A. Schötzau, M. Núñez López, A. Fedier, M. Konantz, T. Vlajnic, D. Calabrese, C.
1006 Lengerke, L. David, B. Rothen-Rutishauser, F. Jacob, V. Heinzelmann-Schwarz, Collagen-rich
1007 omentum is a premetastatic niche for integrin α2-mediated peritoneal metastasis., *eLife* **9** (2020),
1008 doi:10.7554/eLife.59442.

1009 77. T. R. Henry, J. M. Spitsbergen, M. W. Hornung, C. C. Abnet, R. E. Peterson, Early life stage
1010 toxicity of 2,3,7,8-tetrachlorodibenzo-p-dioxin in zebrafish (Danio rerio)., *Toxicol. Appl.*
1011 *Pharmacol.* **142**, 56–68 (1997).

1012 78. G. E. Elonen, R. L. Spehar, G. W. Holcombe, R. D. Johnson, J. D. Fernandez, R. J. Erickson,
1013 J. E. Tietge, P. M. Cook, Comparative toxicity of 2,3,7,8-tetrachlorodibenzo- *p* -dioxin to seven
1014 freshwater fish species during early life-stage development, *Environ. Toxicol. Chem.* **17**, 472–483
1015 (1998).

1016 79. F. Jacob, R. Guertler, S. Naim, S. Nixdorf, A. Fedier, N. F. Hacker, V. Heinzelmann-Schwarz,
1017 Careful selection of reference genes is required for reliable performance of RT-qPCR in human
1018 normal and cancer cell lines., *PLoS ONE* **8**, e59180 (2013).

1019 80. R. Casanova, S. Xu, S. Sivapatham, A. Jacobs, S. Engler, Tumor Profiler Consortium, M. P.
1020 Levesque, R. Dummer, B. Bodenmiller, S. Chevrier, Standardization of suspension and imaging
1021 mass cytometry readouts for clinical decision making, *BioRxiv* (2023),
1022 doi:10.1101/2023.03.19.531228.

1023 81. N. Kotecha, P. O. Krutzik, J. M. Irish, Web-based analysis and publication of flow cytometry
1024 experiments., *Curr. Protoc. Cytom.* **Chapter 10**, Unit10.17 (2010).

1025 82. A. Dobin, C. A. Davis, F. Schlesinger, J. Drenkow, C. Zaleski, S. Jha, P. Batut, M. Chaisson,
1026 T. R. Gingeras, STAR: ultrafast universal RNA-seq aligner., *Bioinformatics* **29**, 15–21 (2013).

1027 83. M. I. Love, W. Huber, S. Anders, Moderated estimation of fold change and dispersion for
1028 RNA-seq data with DESeq2., *Genome Biol.* **15**, 550 (2014).

1029 84. M. E. Ritchie, B. Phipson, D. Wu, Y. Hu, C. W. Law, W. Shi, G. K. Smyth, limma powers
1030 differential expression analyses for RNA-sequencing and microarray studies., *Nucleic Acids Res.*
1031 **43**, e47 (2015).

1032 85. S. Hänzelmann, R. Castelo, J. Guinney, GSVA: gene set variation analysis for microarray and
1033 RNA-seq data., *BMC Bioinformatics* **14**, 7 (2013).

1034

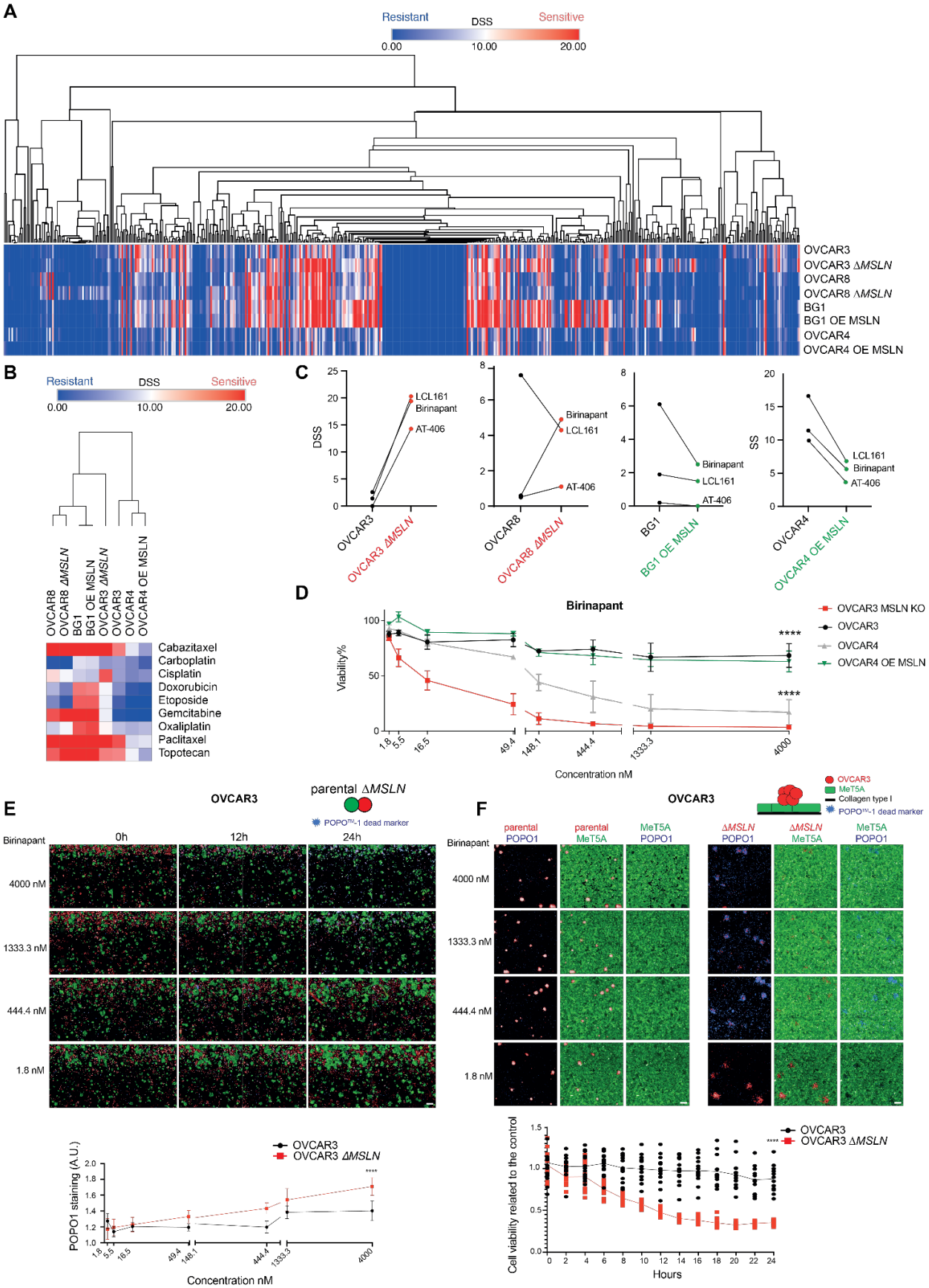
A
Resistant
DSS
Sensitive
0.00
10.00
20.00
OVCAR3
OVCAR3 ΔMSLN
OVCAR8
OVCAR8 ΔMSLN
BG1
BG1 OE MSLN
OVCAR4
OVCAR4 OE MSLN
B
Cabazitaxel
Carboplatin
Cisplatin
Doxorubicin
Etoposide
Gemcitabine
Oxaliplatin
Paclitaxel
Topotecan
C
DSS
SS
LCL161
Birinapant
AT-406
D
Birinapant
Viability%
Concentration nM
OVCAR3 MSLN KO
OVCAR3
OVCAR4
OVCAR4 OE MSLN
E
OVCAR3
parental ΔMSLN
Birinapant
0h
12h
24h
4000 nM
1333.3 nM
444.4 nM
1.8 nM
POPO1 staining (A.U.)
Concentration nM
F
OVCAR3
MeT5A
Collagen type I
parental POPO1
parental MeT5A
MeT5A POPO1
ΔMSLN POPO1
ΔMSLN MeT5A
Cell viability related to the control
Hours

1038 **Figure 1. SMAC mimetics selectively target MSLN^{low} EOC cell lines. *A.*** Heatmap depicting
1039 heterogeneous drug responses using a library of 528 compounds tested across 8 EOC cell lines
1040 with (Δ*MSLN for knockout; OE for overexpression*) and without genetic manipulation of MSLN
1041 expression. The represented values are drug sensitivity scores (DSS) colors indicating either
1042 sensitivity (red) or resistance (blue). **B.** Heatmap with drug responses of chemotherapeutic
1043 compounds commonly applied in EOC treatment. Visualization and hierarchical clustering of rows
1044 (1-Person correlation) was performed using Morpheus software. **C.** Dot plot illustrating the
1045 enhanced effectiveness of SMAC mimetics in cell lines characterized by low MSLN expression.
1046 **D**. Dose-response curves for birinapant across 4 different EOC cell lines. The data presented is
1047 the result of two independent experiments conducted in quadruplicate. **E.** Representative
1048 fluorescence images and quantification of a co-culture system using parental (EGFP) and Δ*MSLN*
1049 (dTomato) OVCAR3 cells treated with an increasing concentration of birinapant. The
1050 corresponding line chart summarizes the quantification of POPO™-1 iodide staining intensity after
1051 48 hours of birinapant treatment. Scale bar 50µm. **F.** Representative fluorescent images of the
1052 mesothelial clearance assay in parental (left) and Δ*MSLN* (right) OVCAR3 cells with and without
1053 birinapant treatment. Cell viability was calculated based on POPO™-1 Iodide staining intensity
1054 and normalized against controls. Data is presented as mean ± SD of two independent
1055 experiments done in quadruplicate (D, E) or sextuplicates (F) *p* values were determined using
1056 two-way ANOVA followed by Sidak's multiple comparison test. (*, $p < 0.05$, ***, $p < 0.001$, ****
1057 $p < 0.0001$). Scale bar 50µm.
1058

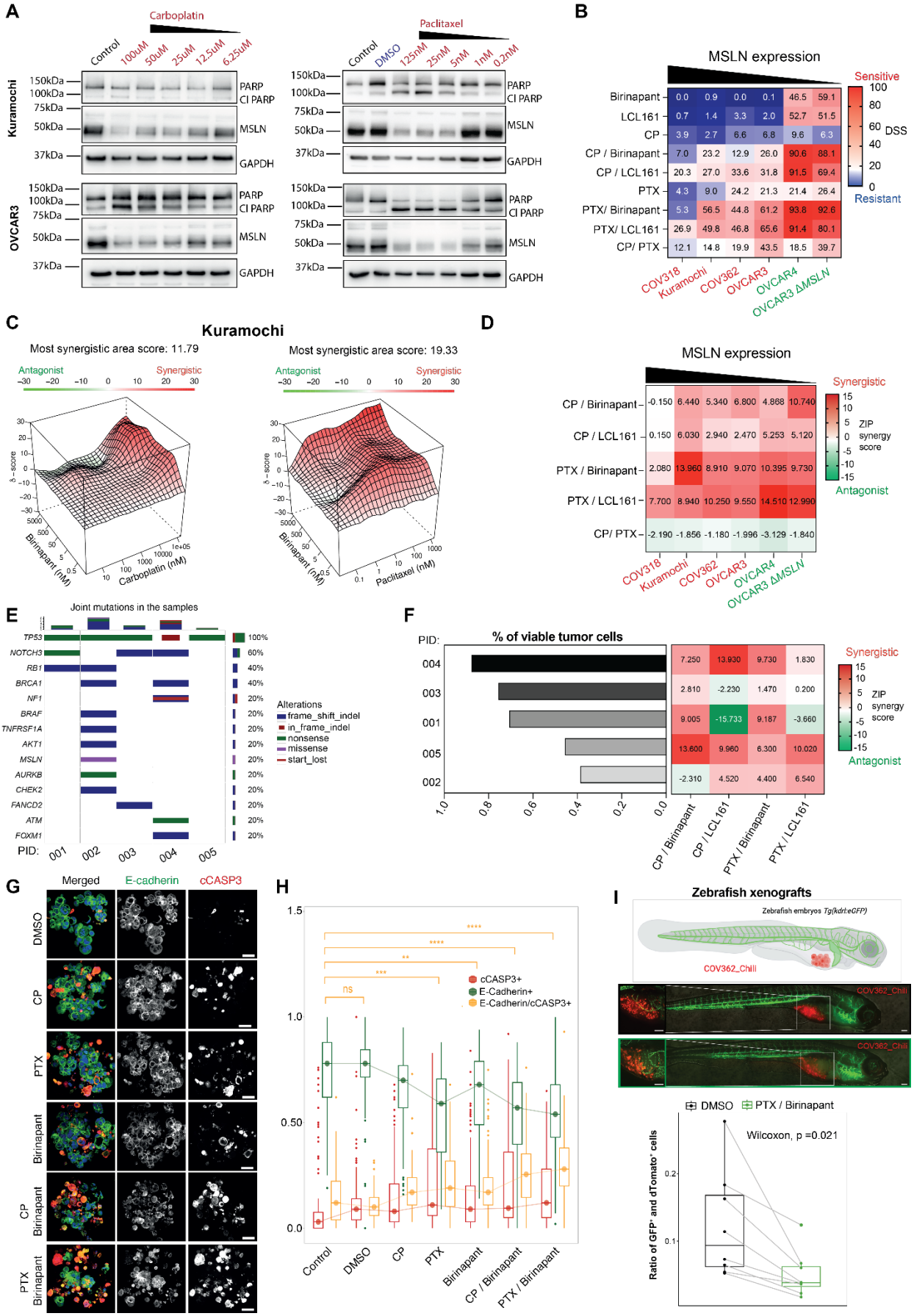
A
Carboplatin
Control
100uM
50uM
25uM
12.5uM
6.25uM
Paclitaxel
Control
DMSO
125nM
25nM
5nM
1nM
0.2nM
Kuramochi
OVCAR3
150kDa
100kDa
75kDa
50kDa
37kDa
PARP
Cl PARP
MSLN
GAPDH
B
MSLN expression
Sensitive
Resistant
DSS
Birinapant
LCL161
CP
CP / Birinapant
CP / LCL161
PTX
PTX/ Birinapant
PTX/ LCL161
CP/ PTX
COV318
Kuramochi
COV362
OVCAR3
OVCAR4
OVCAR3 ΔMSLN
C
Kuramochi
Most synergistic area score: 11.79
Most synergistic area score: 19.33
Antagonist
Synergistic
δ – score
Birinapant (nM)
Carboplatin (nM)
Paclitaxel (nM)
D
MSLN expression
Synergistic
Antagonist
ZIP synergy score
E
Joint mutations in the samples
TP53
NOTCH3
RB1
BRCA1
NF1
BRAF
TNFRSF1A
AKT1
MSLN
AURKB
CHEK2
FANCD2
ATM
FOXM1
PID:
001
002
003
004
005
Alterations
frame_shift_indel
in_frame_indel
nonsense
missense
start_lost
F
% of viable tumor cells
PID:
004
003
001
005
002
CP / Birinapant
CP / LCL161
PTX / Birinapant
PTX / LCL161
Synergistic
Antagonist
ZIP synergy score
G
Merged
E-cadherin
cCASP3
DMSO
CP
PTX
Birinapant
CP Birinapant
PTX Birinapant
H
cCASP3+
E-Cadherin+
E-Cadherin/cCASP3+
ns
Control
DMSO
CP
PTX
Birinapant
CP / Birinapant
PTX / Birinapant
I
Zebrafish xenografts
Zebrafish embryos Tg(kdrl:eGFP)
COV362_Chili
DMSO
PTX / Birinapant
Wilcoxon, p =0.021
Ratio of GFP+ and dTomato+ cells

1059

1060 **Figure 2. SMAC mimetics enhance chemotherapy sensitivity. A.** Representative Western
1061 blots depicting reduction of MSLN following exposure to carboplatin and paclitaxel in Kuramochi
1062 and OVCAR3 cells. **B.** Heatmap with increasing DSS values for the combination of SMAC
1063 mimetics with either carboplatin or paclitaxel across six EOC cell lines, sorted by MSLN
1064 expression levels. **C** and **D.** Synergy scores for SMAC mimetics in combination with either
1065 carboplatin or paclitaxel. **E.** Oncoprint for HGSOC samples treated *ex vivo*. Matched genomic
1066 data obtained from whole-exome sequencing, only genes with alterations in at least one patient
1067 sample are visualized. **Supplementary Table 3**. **F.** Tumor content and matched synergy scores
1068 for SMAC mimetics in combination with either carboplatin or paclitaxel in HGSOC patient-derived
1069 cells. **G** and **H.** Representative immunofluorescent images and quantification of "on target" tumor
1070 effect of the different treatments using an *ex vivo* culture system in three HGSOC samples.
1071 Carboplatin, paclitaxel, and birinapant were used at the final concentration of 10μM, 10nM, and
1072 500nM, respectively. At least 20 cell aggregates were imaged and quantified for each condition
1073 in each patient sample resulting in 122,805 cells analyzed. Scale bar 50 μm. *P* values were
1074 determined using the Wilcoxon comparison test *, $p < 0.05$, ***, $p < 0.001$, **** $p < 0.0001$. **I.**
1075 Representative immunofluorescent images and quantification of COV362-Chili zebrafish
1076 xenografts, demonstrating a reduction in live COV362-Chili cells after 72 hours of exposure to the
1077 combination of birinapant (5000nM) with paclitaxel (1000nM). Data presented as a result of three
1078 independent experiments, each done in duplicate, *p* values were determined using the Wilcoxon
1079 comparison test. Scale bar 100μm.

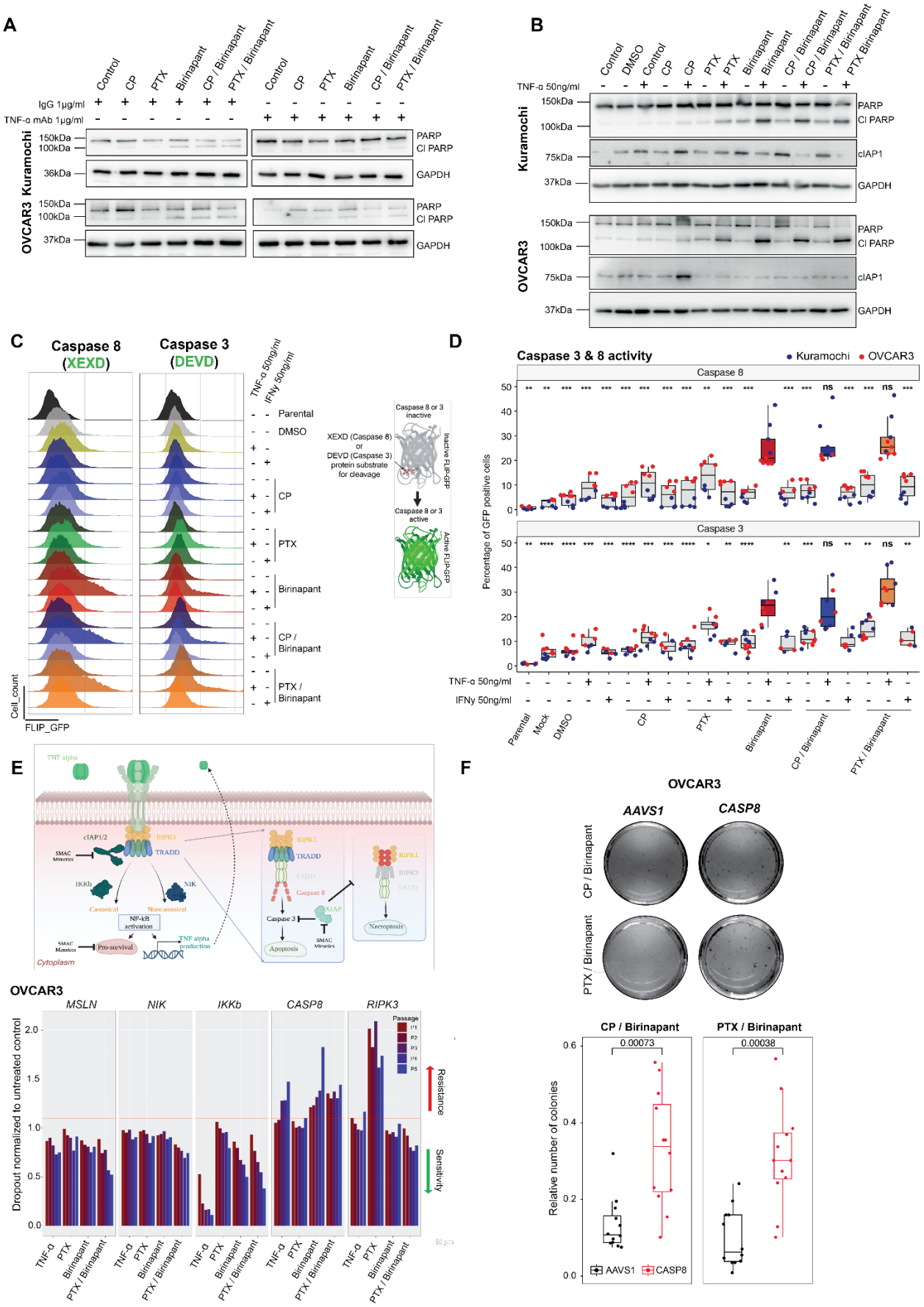
A
Control
CP
PTX
Birinapant
CP / Birinapant
PTX / Birinapant
IgG 1μg/ml
TNF-α mAb 1μg/ml
Kuramochi
OVCAR3
150kDa
100kDa
36kDa
37kDa
PARP
Cl PARP
GAPDH
B
DMSO
TNF-α 50ng/ml
cIAP1
75kDa
C
Caspase 8
(XEXD)
Caspase 3
(DEVD)
TNF-α 50ng/ml
IFNγ 50ng/ml
Parental
DMSO
CP
PTX
Birinapant
CP / Birinapant
PTX / Birinapant
Cell_count
FLIP_GFP
Caspase 8 or 3 inactive
XEXD (Caspase 8) or DEVD (Caspase 3) protein substrate for cleavage
Inactive FLIP-GFP
Caspase 8 or 3 active
Active FLIP-GFP
D
Caspase 3 & 8 activity
Kuramochi
OVCAR3
Caspase 8
Caspase 3
Percentage of GFP positive cells
TNF-α 50ng/ml
IFNγ 50ng/ml
Parental
Mock
DMSO
CP
PTX
Birinapant
CP / Birinapant
PTX / Birinapant
E
TNF alpha
cIAP1/2
RIPK1
TRADD
SMAC Mimetics
IKKb
NIK
Canonical
Noncanonical
NF-kB activation
Pro-survival
TNF alpha production
Cytoplasm
FADD
Caspase 8
Caspase 3
XIAP
Apoptosis
RIPK3
Necroptosis
OVCAR3
MSLN
NIK
IKKb
CASP8
RIPK3
Passage
P1
P2
P3
P4
P5
Dropout normalized to untreated control
Resistance
Sensitivity
TNF-α
PTX
Birinapant
PTX / Birinapant
F
OVCAR3
AAVS1
CASP8
CP / Birinapant
PTX / Birinapant
Relative number of colonies
0.00073
0.00038
AAVS1
CASP8

1082 **Figure 3. Birinapant restores the apoptotic effect of chemotherapy in a TNFα-dependent**
1083 **manner. A** and **B.** Representative Western blots demonstrate the TNFα dependency for the
1084 enhanced efficacy of birinapant in combination with either carboplatin or paclitaxel in Kuramochi
1085 and OVCAR3 cell lines after 24 hours. Carboplatin, paclitaxel, and birinapant were used at the
1086 final concentration of 10μM, 10nM, and 500nM, respectively. **C** and **D**. Representative histograms
1087 and quantification of a real-time apoptosis reporter assay using FLIP-GFP as a readout supporting
1088 the specificity of TNFα in increasing cell apoptosis mediated through caspase 8 and 3 when
1089 combined with birinapant, and birinapant in combination with either carboplatin or paclitaxel.
1090 Carboplatin, paclitaxel, and birinapant were used at the final concentration of 10μM, 10nM, and
1091 500nM, respectively. The data presented is the result of at least three independent experiments.
1092 *P* values were determined by Wilcoxon comparison, * $p < 0.05$, ***, $p<0.001$, **** $p<0.0001$. **E.**
1093 Illustration of TNFα signaling pathway and histograms for CRISPR-Cas9 cell competition assay
1094 over five consecutive passages depicting increased resistance and sensitivity across different
1095 treatments upon gene editing of *MSLN* and TNFα pathways-related genes *NIK*, *IKKb, CASP8,*
1096 and *RIPK3***. F.** Colony formation assay with quantified colonies to assess treatment-dependent
1097 survival upon deletion of *AAVS1* (negative control) or *CASP8* in OVCAR3-Cas9^{+} cells.
1098 Carboplatin, paclitaxel, and birinapant were used at the final concentration of 1μM, 1nM, and 5nM,
1099 respectively. The data presented is the result of two independent experiments done in triplicates.
1100 *P* values were determined by Wilcoxon comparison test.

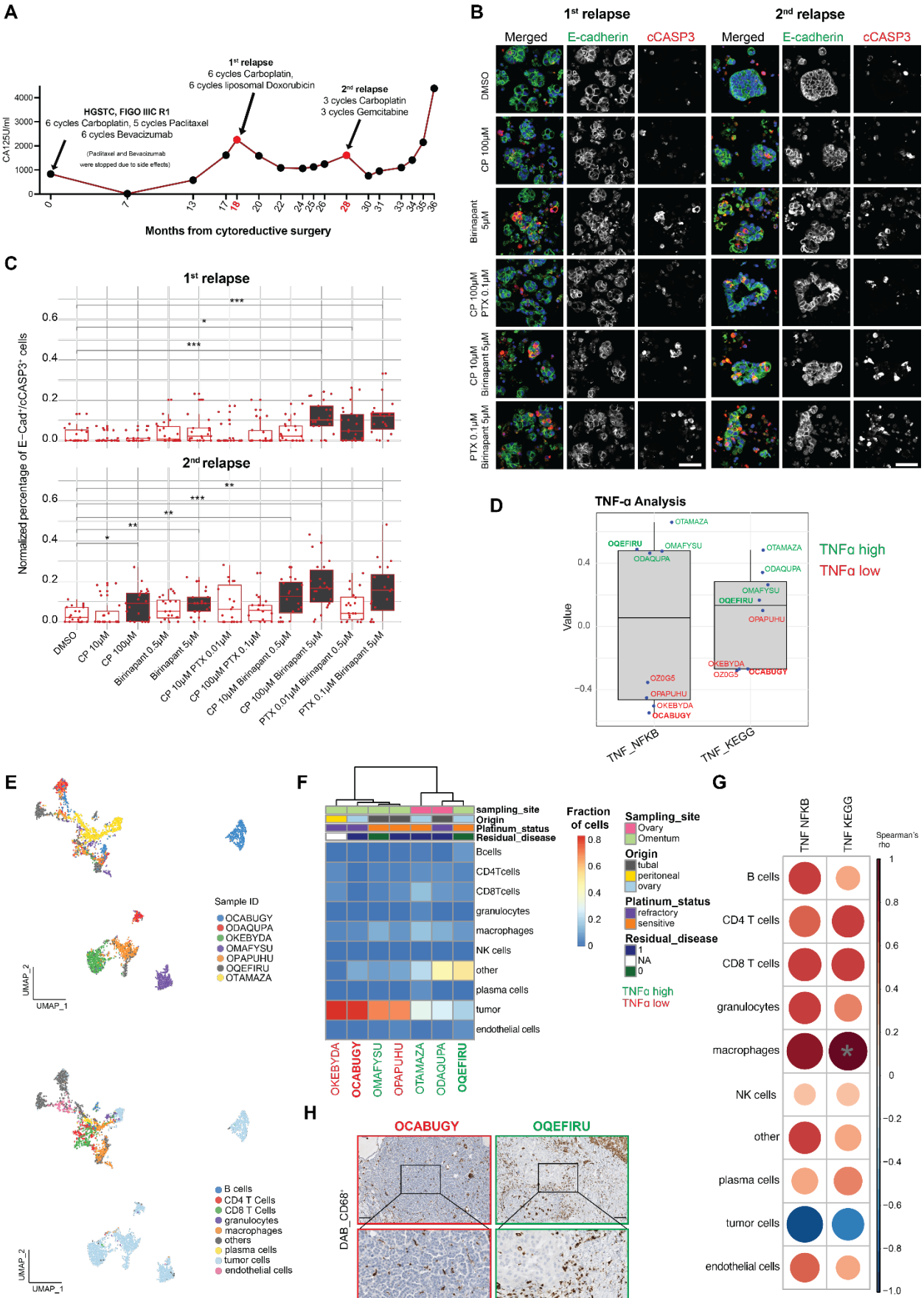
A
1st relapse
6 cycles Carboplatin,
6 cycles liposomal Doxorubicin
2nd relapse
3 cycles Carboplatin
3 cycles Gemcitabine
HGSTC, FIGO IIIC R1
6 cycles Carboplatin, 5 cycles Paclitaxel
6 cycles Bevacizumab
(Paclitaxel and Bevacizumab were stopped due to side effects)
CA125U/ml
Months from cytoreductive surgery
B
1st relapse
2nd relapse
Merged
E-cadherin
cCASP3
DMSO
CP 100μM
Birinapant 5μM
CP 100μM PTX 0.1μM
CP 10μM Birinapant 5μM
PTX 0.1μM Birinapant 5μM
C
1st relapse
2nd relapse
Normalized percentage of E-Cad+/cCASP3+ cells
DMSO
CP 10μM
CP 100μM
Birinapant 0.5μM
Birinapant 5μM
CP 10μM PTX 0.01μM
CP 100μM PTX 0.1μM
CP 10μM Birinapant 0.5μM
CP 100μM Birinapant 5μM
PTX 0.01μM Birinapant 0.5μM
PTX 0.1μM Birinapant 5μM
D
TNF-α Analysis
Value
TNF_NFKB
TNF_KEGG
TNFα high
TNFα low
OTAMAZA
OQEFIRU
OMAFYSU
ODAQUPA
OPAPUHU
OZ0G5
OKEBYDA
OCABUGY
E
Sample ID
OCABUGY
ODAQUPA
OKEBYDA
OMAFYSU
OPAPUHU
OQEFIRU
OTAMAZA
UMAP_1
UMAP_2
B cells
CD4 T Cells
CD8 T Cells
granulocytes
macrophages
others
plasma cells
tumor cells
endothelial cells
F
sampling_site
Origin
Platinum_status
Residual_disease
Bcells
CD4Tcells
CD8Tcells
granulocytes
macrophages
NK cells
other
plasma cells
tumor
endothelial cells
Fraction of cells
Sampling_site
Ovary
Omentum
Origin
tubal
peritoneal
ovary
Platinum_status
refractory
sensitive
Residual_disease
1
NA
0
TNFα high
TNFα low
G
TNF NFKB
TNF KEGG
Spearman's rho
B cells
CD4 T cells
CD8 T cells
granulocytes
macrophages
NK cells
other
plasma cells
tumor cells
endothelial cells
H
OCABUGY
OQEFIRU
DAB_CD68+

1101

1102 ***Figure 4.*** **Macrophages in the TME promote TNFα pathway activation in HGSOC samples.**
1103 **A.** Serum levels of CA125 in a patient with HGSOC during 36 months of follow-ups**. B** and **C.**
1104 Representative immunofluorescence images and box plots depicting increased cancer cell
1105 apoptosis (% of E-cadherin, cCASP3 positive cells) after exposure to birinapant in combination
1106 with either carboplatin or paclitaxel. At least 20 cell aggregates were imaged and quantified for
1107 each condition in each sample, in a total of 47'413 cells were analyzed. Scale bar 50µm. *P* values
1108 were determined by the Wilcoxon comparison test. **p* <0.05, ***p* <0.01, ****p*<0.001. **D.** Pathway
1109 activation scores (z-scored) for neoadjuvant HGSOC-derived patient samples (n=8) with
1110 correction for the tumor content determined by CyTOF. Data generated from bulk RNAseq**. E.**
1111 UMAPs depicting the major cell type composition across seven different HGSOC samples using
1112 IMC. **F** and **G**. Heatmap and correlation matrix showing a significant association of macrophage
1113 abundance and TNF*α* -related pathways activation. A grey asterisk indicates significant
1114 correlations (r=0.82, *p*=0.034). **H.** Representative immunohistochemistry stainings in HGSOC
1115 samples with high and low CD68 cellular content. Scale bar 100µm.
1116

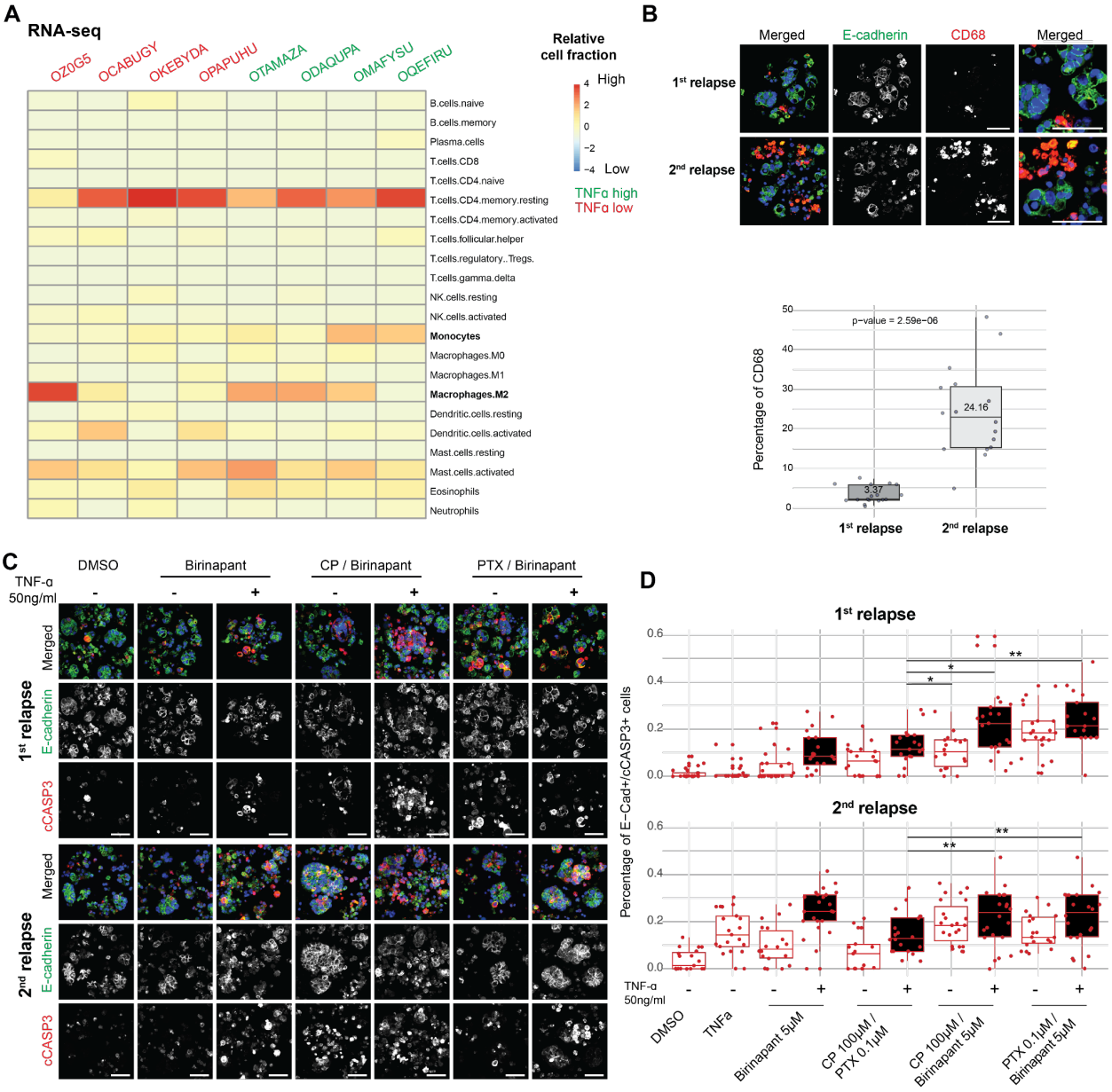
A
RNA-seq
OZ0G5
OCABUGY
OKEBYDA
OPAPUHU
OTAMAZA
ODAQUPA
OMAFYSU
OQEFIRU
B.cells.naive
B.cells.memory
Plasma.cells
T.cells.CD8
T.cells.CD4.naive
T.cells.CD4.memory.resting
T.cells.CD4.memory.activated
T.cells.follicular.helper
T.cells.regulatory..Tregs.
T.cells.gamma.delta
NK.cells.resting
NK.cells.activated
Monocytes
Macrophages.M0
Macrophages.M1
Macrophages.M2
Dendritic.cells.resting
Dendritic.cells.activated
Mast.cells.resting
Mast.cells.activated
Eosinophils
Neutrophils
Relative cell fraction
High
Low
TNFα high
TNFα low
B
Merged
E-cadherin
CD68
Merged
1st relapse
2nd relapse
p-value = 2.59e-06
Percentage of CD68
24.16
3.37
1st relapse
2nd relapse
C
DMSO
Birinapant
CP / Birinapant
PTX / Birinapant
TNF-α 50ng/ml
Merged
E-cadherin
cCASP3
1st relapse
2nd relapse
D
1st relapse
2nd relapse
Percentage of E-Cad+/cCASP3+ cells
TNF-α 50ng/ml
DMSO
TNFa
Birinapant 5μM
CP 100μM / PTX 0.1μM
CP 100μM / Birinapant 5μM
PTX 0.1μM / Birinapant 5μM

1132 **Figure 5. Macrophages and TNFα enhance response to bimodal treatments *ex vivo*. A.**
1133 Heatmap displaying the enrichment of myeloid cells (monocytes and M2 macrophages) in
1134 samples with higher (green) and low (red) TNFα gene set activation. Data sourced from bulk RNA
1135 sequencing, based on CIBERSORT relative quantification of the immune compartment using
1136 LM22 signature matrix. **B**. Representative immunofluorescence images and corresponding box
1137 plots illustrating increased $CD68^+$ cell percentage in the 2nd relapse as compared with the 1st
1138 relapse in PID_001. Quantification involved at least 16 cell aggregates that were imaged and
1139 analyzed for each condition in every sample, in a total of 3'354 cells analyzed. Scale bar: 50 µm,
1140 *P* values determined by *t*-test. **C** and **D.** Representative immunofluorescence images and box
1141 plots showing increased cancer cell apoptosis (% of E-cad, cCASP3 positive cells) following
1142 bimodal treatments with TNFα supplementation as compared with carboplatin in combination with
1143 paclitaxel. Quantification included ≥ 20 cell aggregates were imaged and quantified for each
1144 condition in each sample, in total 114'048 cells were analyzed. Scale bar: 50 µm. *P* values were
1145 determined by the Wilcoxon comparison test. $*p < 0.05$, $**p < 0.01$.
1146